A Satellite View of the Synoptic-Scale Organization of Cloud Properties in Midlatitude and Tropical Circulation Systems

NGAR-CHEUNG LAU AND MARK W. CRANE

Geophysical Fluid Dynamics Laboratory/NOAA, Princeton University, Princeton, New Jersey

(Manuscript received 15 August 1994, in final form 16 December 1994)

ABSTRACT

The spatial and temporal variability of various cloud types and cloud optical thickness are investigated using daily global analyses produced by the International Satellite Cloud Climatology Project (ISCCP) for the 1983–90 period. The climatological patterns of the relative abundance of individual cloud types are closely related to prevalent circulation regimes. Composite charts at various time lags relative to selected cloudy episodes are used to describe the representative shape and propagation of the local cloud patterns. These satellite-based findings are consistent with published results obtained from analyses of geopotential height and wind data.

The midlatitude baroclinic cyclones along the wintertime storm tracks over the North and South Atlantic, and the summertime synoptic-scale disturbances occurring over the tropical western Pacific, are selected for more in-depth investigation. The variations of different cloud types in the selected sites are examined in conjunction with the concurrent three-dimensional atmospheric structure and dynamical processes, as deduced from the daily operational analyses generated at the European Centre for Medium-Range Weather Forecasts (ECMWF). Results for the extratropical storm track regions are in agreement with traditional conceptual frameworks for the organization of cloud properties near warm and cold frontal zones. These midlatitude cloud patterns are linked to the vertical circulation induced by the advection of temperature and vorticity in developing baroclinic waves. Results for the tropical western Pacific reveal cloud structures similar to those occurring in squall lines, with low-top clouds in advance of the approaching deep convection zone, and high-top, optically thinner cloud elements in the rear anvil region.

The spatial correspondence between composite features obtained from the independent ISCCP and ECMWF analyses lends credence to the reliability of both datasets, especially in regions with sparse in situ observations. The consistency of the ISCCP cloud patterns with the ambient atmospheric structure and dynamics demonstrates the applicability of satellite data products in advancing our understanding of different types of circulation systems.

1. Introduction

The advancements in satellite technology have brought forth new data resources for studying a wide variety of processes in the earth's atmosphere—its radiative balance, thermal characteristics, hydrologic cycle, and space–time variability of different trace constituents. The temporal and spatial resolutions of these satellite observations far exceed those of in situ measurements collected by the conventional rawinsonde network. Judging from the ever increasing use of various satellite products for monitoring and research purposes during the past three decades, it can be anticipated that innovative diagnosis and interpretation of the voluminous amount of satellite information will play a critical role in expanding our knowledge of the climate system.

The satellite research community has devoted considerable effort to the documentation and understanding of the space–time evolution of various cloud-related optical properties. The International Satellite Cloud Climatology Project (ISCCP), being the first project launched by the World Climate Research Programme, is aimed at systematically providing a multiyear and global coverage of different cloud parameters based on satellite measurements for the 1980s and beyond (Schiffer and Rossow 1983). The array of ISCCP cloud datasets has found wide application, including investigations of tropical deep convective clouds (Fu et al. 1990, 1994), near-equatorial low stratiform clouds (Deser et al. 1993), effects of cloud types on the earth's radiative balance (Ockert-Bell and Hartmann 1992; Hartmann et al. 1992), temperature dependence of cloud optical thickness (Tselioudis et al. 1992), climatological cloud statistics (Weare 1993), reliability of cloud detection algorithms (Rossow and Garder 1993b), and the relationship between cloud properties and sea surface temperature variations (Weare 1994).

It is well known that a substantial portion of atmospheric variability on synoptic timescales (i.e., periods of several days) is attributable to the prevalence of dis-

Corresponding author address: Dr. Ngar-Cheung Lau, GFDL/ NOAA, Princeton University, P.O. Box 308, Princeton, NJ 08542.

TABLE 1. Classification of cloud types according to cloud-top pressure and cloud optical thickness.

	Cloud-top pressure (mb)	Cloud optical thickness			
		0–3.6	3.6–9.4	9.4–23	23–125
High top	50–310	←——high top/thin——→		high top/medium	high top/thick
	310–440	high top/thin	←——high top/medium——→		high top/thick
Middle top	440–680	←——middle top/thin——→		←——middle top/thick——→	
Low top	680–1000	low top/thin	←——low top/thick——→		

tinct types of circulation systems. Notable examples of these meteorological features are the migratory cyclones and anticyclones over the midlatitude oceans, and summertime disturbances in the tropical zone. With the availability of gridded analyses of the observed global wind, temperature, and pressure fields from various operational forecasting centers, considerable progress has been made in the understanding of the structural and dynamical properties of synoptic disturbances residing in the extratropics (e.g., Blackmon et al. 1977; Wallace et al. 1988; Trenberth 1991) and low latitudes (e.g., Nitta and Takayabu 1985; Nitta et al. 1985; Reed et al. 1988; Lau and Lau 1990, 1992). Our empirical and theoretical knowledge of weather systems and their interaction with cloud processes have recently been summarized in the textbooks by Bluestein (1992, 1993), Houze (1993), and Emanuel (1994). The association of these atmospheric phenomena with distinctive signatures of various cloud types has been noted by Troup and Streten (1972) and Evans et al. (1994), among others. Thus far, the relationships between the cloud fields and various types of circulation systems have been examined mostly on the basis of qualitative interpretations of satellite images, or intensive field programs of limited duration and geographical extent. The objective gridded analyses of various cloud properties produced by ISCCP for the whole globe, with space–time resolutions comparable to those of the operational analyses of other meteorological variables, offer an unprecedented opportunity for systematic investigations of the detailed organization of the cloud properties in different kinds of weather disturbances.

The motivation of the present study is to demonstrate that inferences drawn from the ISCCP cloud products are consistent with our dynamical knowledge of synoptic-scale atmospheric behavior in various regional and seasonal contexts. Moreover, we shall explore the degree to which modern satellite observations could augment conventional data resources (such as wind and temperature analyses) in providing a fuller description of different classes of circulation systems. The results to be presented here also serve to cross-validate ISCCP cloud datasets and operational analyses of other meteorological fields.

The above goals are met by analyzing the ISCCP products using techniques analogous to those previously designed for geopotential height and wind fields. The results of these analyses are shown in sections 3 and 4, which offer a global survey of the seasonal climatology of various cloud types, as well as the temporal variability, propagation, and degree of waviness of cloud optical thickness. On the basis of these findings, the extratropical wintertime cyclone waves over the North and South Atlantic, as well as the summertime synoptic disturbances over the tropical western Pacific, are selected for more in-depth scrutiny. For each of the circulation features chosen here, the ISCCP cloud data are overlaid on contemporaneous dynamical and thermodynamical fields generated by the European Centre for Medium-Range Weather Forecasts (ECMWF), so as to delineate the relationships between the three-dimensional distribution of various cloud types and the ambient atmospheric flow structure (see results presented in sections 5 and 6).

2. Datasets

The variations of cloud properties examined in this study are derived from the stage C1 dataset produced by ISCCP. The details of the ISCCP cloud detection algorithms and the data products available have been documented by Rossow et al. (1988), Rossow and Schiffer (1991), and Rossow and Garder (1993a). The C1 data files provide information on various characteristics of satellite image pixels, as inferred from a cloud analysis procedure consisting of three main steps: cloud detection, radiative model analysis, and statistical analysis. Such information is grouped into equal-area grid cells with dimensions of about 280 km in both the zonal and meridional directions. The data values for these cells are transferred to an array with uniform latitude and longitude intervals of 2.5°. These cloud analyses are generated up to eight times per day. The C1 products are available for the period from July 1983 through December 1990. Among the 132 cloud parameters archived in this dataset, we shall focus our attention on the space–time variability of different cloud types, and of the total cloud optical thickness (hereafter referred to as τ). The τ value assigned to each equal-area grid

cell is obtained by a weighted average of the optical thicknesses for individual cloudy pixels identified in that cell. In this averaging procedure, equal weights are given to pixels with albedo values lying in the same (equally spaced) intervals (Rossow and Schiffer 1991).

The cloud type assigned to each image pixel is determined by the altitude of the cloud-top level and the τ value for that pixel (see Table 1). In the present classification scheme, the ranges of cloud-top level and τ for each cloud type are the same as those used by Rossow and Schiffer (1991). Henceforth, we shall refer to various cloud types directly according to their top altitude and τ (e.g., high top/thin, low top/thick, etc.), rather than by using conventional descriptive names (e.g., cirrus, stratus, etc.) Our nomenclature system is intended to avoid any potential confusion between cloud properties inferred from satellite platforms and cloud-type identifications made from the earth's surface. In particular, the satellite cloud classification scheme is based on cloud-top altitude and τ, whereas the cloud-base altitude and visual appearance as determined from ground observations have traditionally been used in defining the cloud morphology (see Houze 1993, chapter 1, for further details).

For a given grid cell, the fractional cover by each cloud type is obtained by dividing the number of pixels satisfying the cloud-top altitude–τ criteria for that cloud type by the total number of pixels being analyzed. Since τ and cloud-type determinations require analysis of satellite measurements in both the infrared and visible channels, these cloud parameters are reported during the daytime hours only. In the present study, the daytime values for a given 24-h period have been arithmetically averaged to form daily means. In view of the limited visible channel measurements in the polar zone during the winter season, and difficulties in detecting clouds over snow-or ice-covered surfaces, we shall analyze the cloud data for regions situated equatorward of 60°N and 60°S only.

While interpreting the vertical distributions of cloud amounts, it must be borne in mind that satellite observations tend to underestimate the amount of any existing clouds in lower layers whenever high clouds are present. In such situations, the satellite instruments, which take measurements from a vantage point above the multiple cloud decks, would report the presence of the topmost cloud type, whereas the lower-level clouds would remain undetected. It is also probable that the cloud retrieval algorithms might interpret a multilayer cloud scene as a single, optically thick cloud deck situated at high altitudes.

The structure of the atmospheric circulation is inferred from the twice-daily, global analyses of horizontal wind, pressure velocity, temperature, relative humidity, and geopotential height at 1000, 850, 700, 500, 300, 200, and 100 mb, as produced by the ECMWF on an operational basis. These data grids have a horizontal

resolution of 2.5° in latitude and longitude. The period of ECMWF analyses to be examined here coincides with that covered by the available ISCCP dataset. In analogy to the cloud products, daily means have been computed by averaging the ECMWF analyses for 0000 and 1200 UTC.

3. Cloud-type climatology

The relative abundance of various cloud types in different geographical locations is illustrated in Fig. 1, for the months of (a) October–March, and (b) April–September. The 6-month periods selected here correspond to the warm and cool halves of the annual cycle. Hence each panel in Fig. 1 combines the cloud climatologies for an extreme season (winter or summer) and for portions of the adjoining transition seasons (spring and autumn). In constructing these diagrams, arithmetic time averages of the fractional cover by each of the seven cloud types described in section 2 and Table 1 have been computed. The sides of each 2.5° × 2.5° longitude–latitude grid cell (hereafter referred to as a "box") in these charts are further subdivided into 10 segments, so as to form a matrix consisting of 100 small "elements." The fractional cover by a given cloud type in a box is then indicated by filling a corresponding fraction of the elements in that box with a distinctive color assigned to the cloud type in question (see legend on the right side of the charts). High-top, middle-top, and low-top clouds are denoted by red, yellow, and blue elements, respectively. For cloud decks at a given altitude, thicker (thinner) clouds are indicated by deeper (lighter) shades of the same color. For a given box, the cloud type with the largest fractional cover is highlighted by filling contiguous elements situated around the centroid of that box. The cloud types ranked second to fifth in fractional cover are indicated by filling contiguous elements located near the four corners of the same box. The sixth and seventh ranked cloud types are omitted from this presentation for the sake of clarity. All remaining elements in a box are filled in with black, so as to provide an approximate measure of the relative portion of the cloud-free sky. Note that the lack of data input from the Insat satellite results in some data discontinuities over the Indian Ocean and central Asia.

The patterns in Fig. 1 reveal that the tropical zone extending eastward from the Indian Ocean to the western Pacific is dominated by thin high-top clouds, such as those commonly found in anvils spreading from convective towers. The continental convection over Africa, South America, and Southeast Asia is characterized by thicker high-top or middle-top clouds. The prevalent cloud cover associated with the intertropical convergence zones (ITCZs) off the western coasts of Central America and Africa during the warm season is also characterized by high-top or middle-top clouds of the thicker variety. All of the above tropical features ex-
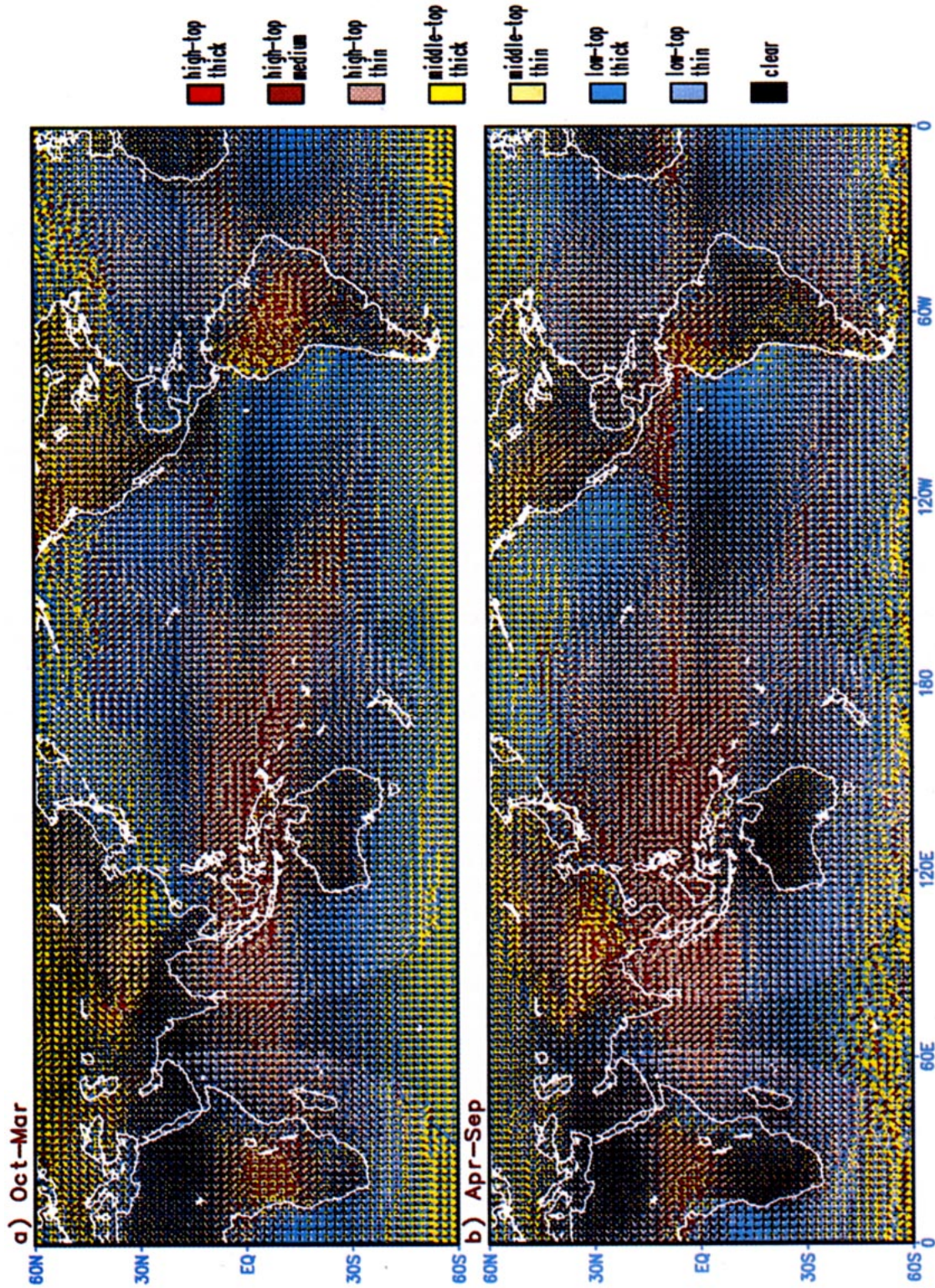
FIG. 1. Climatological distributions of the relative abundance of various cloud types during (a) October–March and (b) April–September. For each 2.5° × 2.5° grid box, the fractional cover by a cloud type is indicated by filling a corresponding fraction of that box with the color designated to the cloud type in question (see legend at right and Table 1). Refer to text for details of the coloring procedure.

hibit marked meridional displacements with the seasons, with more widespread cloudiness in the summer hemisphere. Particularly noteworthy is the prominence of cloudy regions in the South Pacific convergence zone (SPCZ, which extends southeastward off the coast of New Guinea), the South Atlantic convergence zone (protruding southeastward from the Brazilian coast) and the central portion of South America during the local warm season (Fig. 1a), and the summertime cloud cover over the Asian monsoon region as well as the waters surrounding Central America (Fig. 1b).

In the subtropical zone, thick low-top cloud decks extend over the eastern portions of the Pacific and Atlantic in both hemispheres, as well as the southeastern Indian Ocean. These regions of low-top clouds are under the influence of climatological anticyclones at sea level, where dry, subsiding air motion prevails. The low-top cloud regimes over the North Pacific and North Atlantic are broader and better defined during the warm season, in agreement with the surface observations of stratiform clouds described by Klein and Hartmann (1993). The major subtropical deserts of Sahara, southwestern Asia, southern Africa, and Australia are notable for their relatively sparse cloud amounts. Also evident is the almost cloud-free "maritime desert" over the South Pacific, which is bounded by the ITCZ to the north, the SPCZ to the southwest, and the low-top cloud deck to the east. An analogous but smaller cloud-free feature can be seen over the South Atlantic.

Over the extratropical oceans, and especially during the cool season, the abundances of low-top, middle-top, and high-top clouds are comparable to each other. A majority of the maritime clouds in the temperate zone are optically thick. These regions of mixed cloud types are coincident with the preferred trajectories of wave-like baroclinic disturbances, which consist of alternating cyclones and anticyclones (e.g., see Blackmon et al. 1984). The midlatitude skycover over the central and western Eurasian landmass changes from middle-top clouds in the cool season to clouds with lower ceilings in the warm season. The wintertime cloud shield over eastern Siberia consists mainly of thin high-top clouds.

In summary, the seasonal ISCCP climatology of cloud type is consistent with the nature of the prevalent circulation regimes in different parts of the globe. Rossow et al. (1993) have compared the satellite cloud products described here with surface observations compiled by Warren et al. (1986, 1988) and reported overall agreement in the geographical and seasonal variations of cloud amounts deduced from the two independent data sources. Using a format similar to that of Fig. 1, we have plotted the seasonal climatology of various cloud types inferred from the ground-based dataset of Warren et al. The gross features of these charts (not shown) are consistent with those noted in the ISCCP results. The most notable discrepancy between the satellite and surface observations is that the former report

relatively smaller amounts of low-top clouds, probably because such clouds are shielded from the satellite sensors by any cloud cover with ceilings located at a higher altitude. Broad agreement is also noted between the climatological charts in Fig. 1 and those presented by Weare (1992, his Figs. 2 and 3) using Nimbus-7 estimates of cloud height and cloud amount.

4. Characteristics of temporal and spatial variability of cloud properties

We now examine the cloud variability associated with two specific synoptic-scale phenomena: extratropical wintertime cyclones over the North and South Atlantic, and tropical summertime disturbances over the western Pacific. The main rationale for our choices is that the structural and dynamical properties of these circulation systems have already been well documented in various empirical and theoretical studies (see references in the introduction). This solid knowledge base would expedite the validation and physical interpretation of our findings on cloud activity at the selected sites.

a. Time series and frequency distribution function

The time series of daily arithmetic means of cloud optical thickness τ are presented in Fig. 2 for an arbitrarily selected cool season at a grid point situated in the North Atlantic storm track region (at 46°N, 46°W, see inset in the left panel) and for a warm season at a point in the active tropical Pacific zone (at 16°N, 131°E, see inset in the right panel). It is seen that episodes of large τ (with values often reaching 40 and beyond) appear as distinct spikes in the time series for both sites. These intense signals stand out prominently from a background of low τ (typically less than 10). Both the amplitude of the individual episodes and the background level are higher in the extratropics than in the Tropics. The occurrence of events with high τ over the North Atlantic is relatively more frequent and erratic, with peak amplitudes spanning a broad range of τ throughout the cool season. The typical time interval between the outstanding episodes in the extratropics is about 4–7 days, whereas the corresponding period for the tropical Pacific lengthens to more than 10 days. The latter region is also characterized by the almost complete absence of outstanding events in the months of April and May, which precede the arrival of the summer monsoon in the western Pacific. This springtime quiescent period is discernible in the time series for all years covered by the ISCCP dataset.

Also shown in Fig. 2 are the frequency distribution functions (histograms) of the τ values for the cool season in the North Atlantic (left panel) and the warm season in the tropical western Pacific (right panel). These plots are constructed using daily arithmetic means of τ at 20 (15) grid points in the North Atlantic
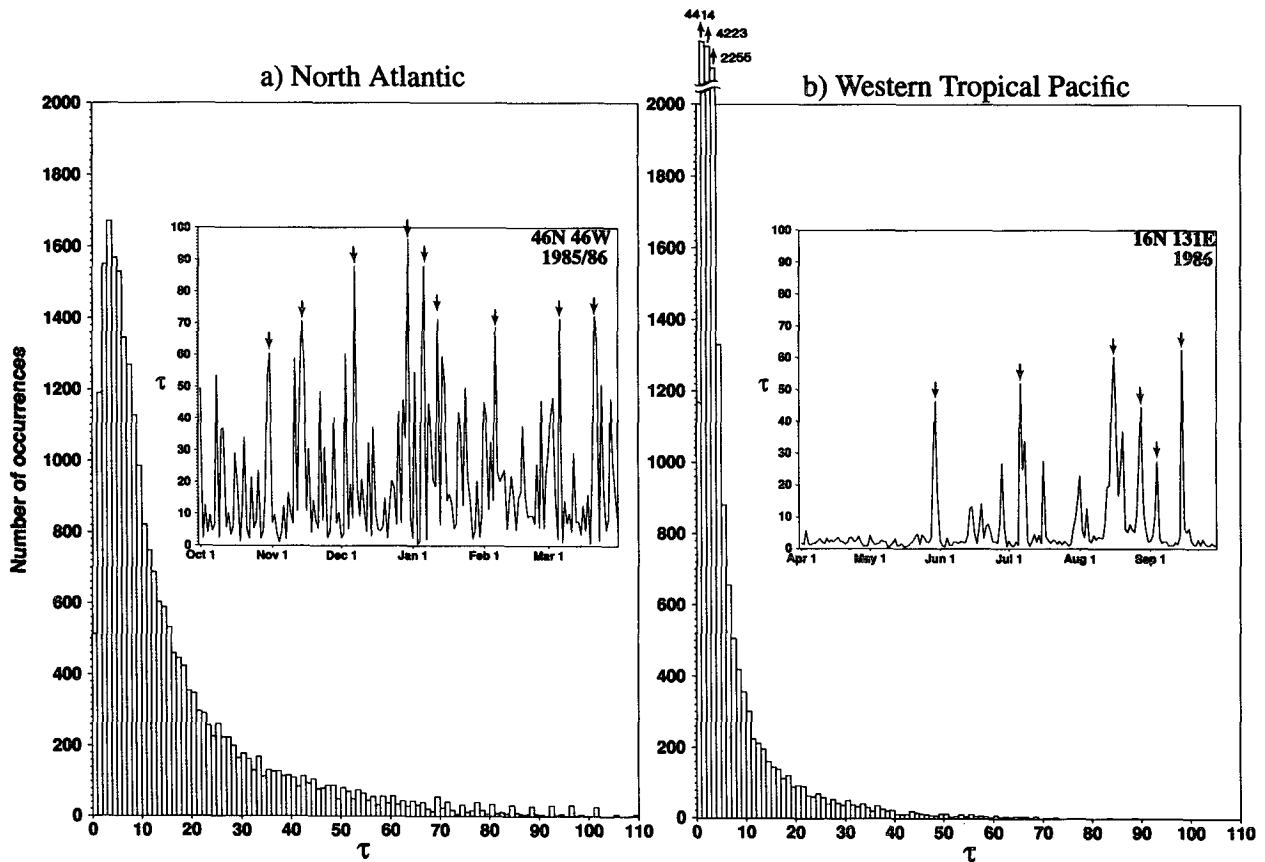
FIG. 2. Frequency distribution of daily means of cloud optical thickness at (a) 20 individual sites in the extratropical North Atlantic (see dots in Fig. 5a) during October–March, and (b) 15 sites in the tropical western Pacific (see dots in Fig. 5c) during April–September, in the 1983–90 period. Each column in the histograms represents the number of occurrences of optical thickness values falling within a given interval (which has a uniform width of one). Inset in the histograms are time series of daily means of cloud optical thickness at 46°N, 46°W during the 1985/86 cool season (left panel), and at 16°N, 131°E during the 1986 warm season (right panel). Pointers in the insets indicate key dates chosen for constructing the composite patterns in Fig. 3.

(tropical Pacific) for the entire 1983–90 period. The grid points used in this computation lie in the vicinity of the site depicted by the time series in the inset, and their precise location will be shown in Fig. 5. The histograms illustrate the number of data points with magnitudes of τ residing in individual "bins" with intervals of one. It is evident from the highly skewed appearance of the frequency distributions for both regions that the variations of τ depart significantly from a symmetric Gaussian probability function. Instead, the gamma distribution, which is commonly used to describe variations of precipitation amounts (e.g., Ison et al. 1971), would provide a better fit to the histograms in Fig. 2. The presence of intermittent events of large τ is depicted by the "tail" in the distribution, which extends to values much larger than the mean of the total population.

In view of the distinctly non-Gaussian character of the frequency distribution of τ, such standard statistical measures as means, variances, covariances, and significance levels for hypothesis testing must be interpreted

with caution. On the other hand, the "spiky" appearance of the time series in Fig. 2 suggests that the outstanding events are best represented as a discrete process being alternately switched on and switched off at sharply defined time instants. The most appropriate tool for diagnosing the properties common to these pulse-like episodes appears to be a composite approach, which entails the identification of those dates on which the prominent episodes occurred, and then averaging the pertinent cloud and circulation fields over the entire set of reference dates. Many of the results to be presented hereafter are based on this composite method, as opposed to those procedures (such as linear correlation) in which every data point in the time series enters into the computation.

b. Composite charts

As an illustration of the basic analysis procedure used in the present study, we first describe how a composite pattern can be constructed with reference to the

time series of τ at a given location. The two reference sites selected for this purpose are identical to those depicted by the time series shown in the insets of Fig. 2. For each 6-month cool season in the 7-yr record available, the nine dates (which amount to about 5% of the 182-day sample) with the largest τ values at the North Atlantic point are identified, thus yielding a total pool of $9 \times 7 = 63$ "key" dates for constructing the composite patterns. As has been noted earlier, the western tropical Pacific is void of outstanding events in April and May. We have thus selected only six dates with the largest τ for each warm season (yielding a total sample of $6 \times 7 = 42$) at this tropical site. To avoid situations in which the outstanding episodes occur too close to each other in time, we require that the key dates for both sites be separated from each other by at least 4 days. In the event that a pair of key dates fail to satisfy this criterion, the date with the lower amplitude is eliminated from the set, and is replaced by another episode in the same season with ranking just below the original nine- or six-member set. The key dates thus selected for the particular year portrayed by the time series in Fig. 2 are denoted by small pointers. It is noteworthy that these dates correspond to events ranking in the 95th percentile and higher. Therefore the principal features appearing in the composite charts of τ (especially those in the vicinity of the reference site) should have a high level of statistical significance.

The composite charts of τ, as constructed by arithmetic averaging over the pool of key dates (hereafter referred to as "day 0") obtained from the above method, are displayed in the middle panels of Fig. 3 for the North Atlantic (left) and western tropical Pacific (right). To delineate the temporal evolution of individual features in these patterns, the composite procedure has been applied to the data for the day before day 0 (hereafter referred to as "day -1," see upper panels), and the day after day 0 ("day $+1$," lower panels). For all patterns shown in Fig. 3, the composite signals are presented as departures from the local background level, which is estimated by averaging the τ values corresponding to days -2, -1, $+1$, and $+2$. Since the τ values jump to unusually high amplitudes on day 0 (see insets in Fig. 2), these data points are specifically excluded from the computation of the background level.

Over the North Atlantic, the area of enhanced τ (red shading) in the vicinity of the reference site on day 0 (Fig. 3b) has a southwest–northeast orientation. The shape of this feature is reminiscent of the familiar cloud shield associated with a typical midlatitude frontal system. Located to the east and the west of this zone of large τ are regions of reduced τ (blue shading, in particular, note the negative extremum marked as N) with a similar southwest–northeast orientation. The characteristic wavelength of this composite pattern, as estimated by the distance between the two centers of reduced τ in Fig. 3b, is approximately 4000–5000 km.

The identities of the principal features on day 0 are maintained on days -1 and $+1$ (Figs. 3a and 3c). These features undergo a systematic eastward displacement within the 48 h considered here. The center of maximum τ moves from the Nova Scotia–Newfoundland area on day -1 (denoted as P_{-1} in Fig. 3a) to the central North Atlantic on day $+1$ (P_{+1} in Fig. 3c). The propagation speed of this phenomenon, as estimated by dividing the distance between P_{-1} and P_{+1} by 2 days, is approximately 15 m s^{-1}.

Over the tropical western Pacific, the center of maximum τ is seen to translate west-northwestward from P_{-1} in Fig. 3d to P_{+1} in Fig. 3f, yielding an average propagation speed of about 5 m s^{-1}. The wavelike signature noted earlier for the North Atlantic phenomena is less evident in the Tropics, with the regions of reduced cloud cover being rather ill defined (e.g., see weak center marked N in Fig. 3e).

c. Propagation vectors and temporal coherence

Individual composite patterns analogous to those shown in Fig. 3 have been computed using each point in a 2.5° latitude × 5° longitude grid mesh as the reference site. For a given reference site P_0, the positive extrema in the composite chart on day -1 (i.e., P_{-1}, see examples in Figs. 3a and 3d) and on day $+1$ (P_{+1}, see Figs. 3c and 3f) are identified. In this and the following subsections, all searches for such extrema are conducted within a domain centered at P_0, and with longitudinal and latitudinal extents of 60° and 30°, respectively. A propagation vector is then assigned to the grid point P_0. The orientation of this vector is determined by the arrow pointing from P_{-1} to P_{+1}. The magnitude of this vector is computed by dividing the distance between P_{-1} and P_{+1} by 2 days. As an indicator of how well the primary cloud signal is maintained during this 2-day period, the average of the magnitude of the composite τ values at P_{-1} and P_{+1} is also evaluated, and is hereafter referred to as the "temporal coherence" for the site P_0.

The near-global distributions of the propagation vectors (arrows) and temporal coherence (color shading), as computed using the method outlined above, are presented in Fig. 4 for the 6-month periods of (a) October–March, and (b) April–September. For the sake of clarity, the zonal and meridional components of the propagation vectors as well as the coherence fields have been smoothed using the nine-point filter described by Holloway (1958, his Fig. 10). The vectors are plotted only over those reference sites with temporal coherences larger than 8.

It is seen from Fig. 4a that the propagation vectors undergo a gradual transition from a predominantly southeastward orientation to a northeastward orientation as they pass over the east Asia–western North Pacific and North America–western North Atlantic sectors. This behavior is apparently associated with the
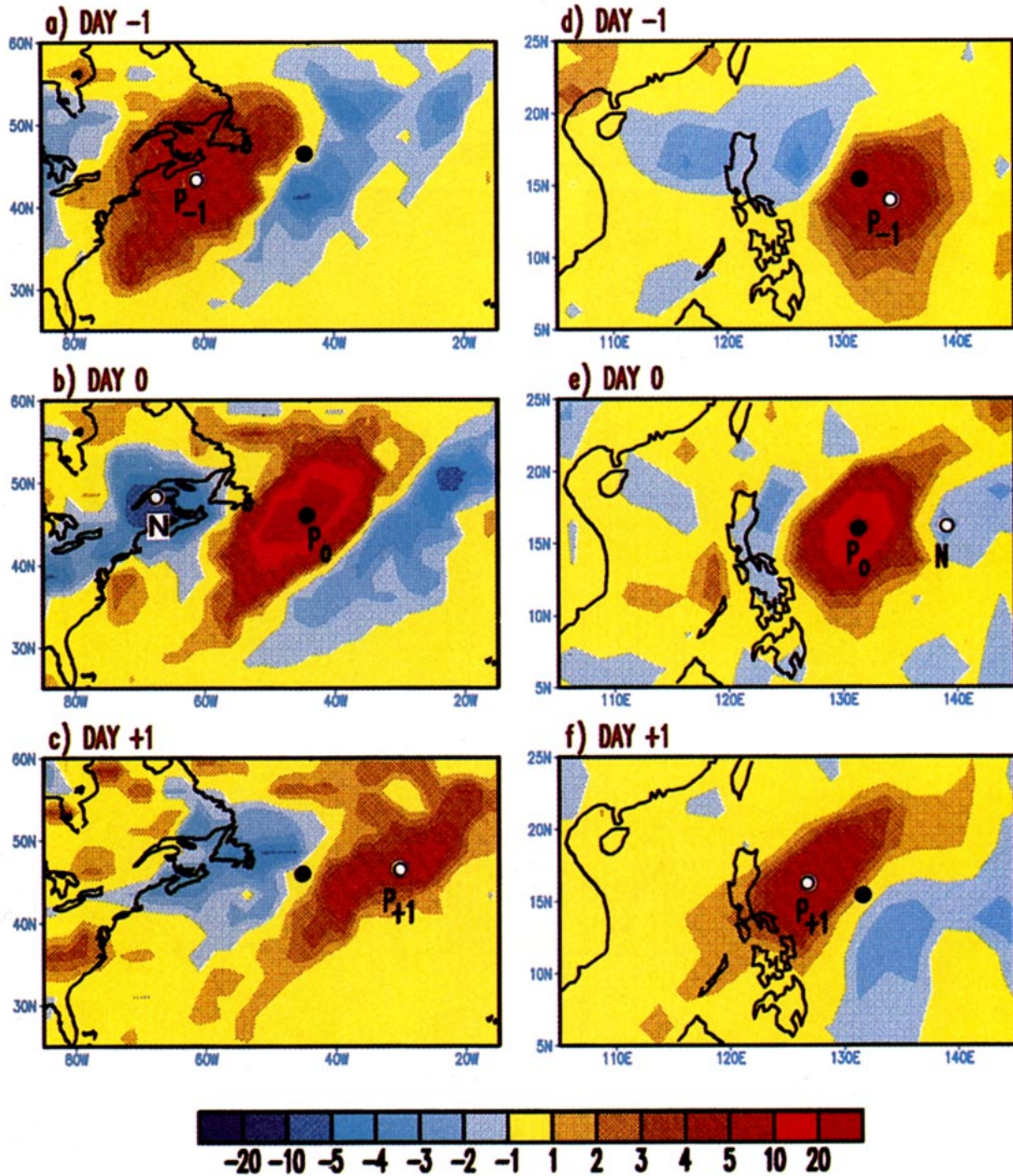
FIG. 3. Composite charts of cloud optical thickness for the North Atlantic region during the cool season (left panels), and for the tropical western Pacific region during the warm season (right panels), as constructed on the basis of outstanding cloudy events at the reference sites 46°N, 46°W and 16°N, 131°E, respectively. Composite patterns for the key dates (when maximum cloud optical thickness occurred) are shown in the middle panels. Patterns for one day before (after) the key dates are shown in the upper (lower) panels. All composite data displayed here (color shading, see scale bar at bottom) represent deviations from a background level estimated by averaging over the values for ±1 and ±2 day lags relative to the key dates. The reference points (solid dots in all panels) are labeled as P_0 in (b) and (e). The positive extrema appearing in the charts for −1 day and +1 day lags (open circles) are labeled as P_{-1} and P_{+1}, respectively. The negative extrema in the charts for the key dates (open circles) are labeled as N. Note that the longitudinal and latitudinal extents of the left panels are larger than those of the right panels by a factor of approximately 2.

advective effects of the upper-level stationary wave troughs residing in these regions during the cool season (e.g., see Schubert et al. 1990a, p. 174). Similarly, the change from northeastward to southeastward propaga-

tion over eastern North Atlantic/Europe and eastern North Pacific/western North America corresponds well with the local stationary wave ridges. The propagation speed over the western portions of the North Pacific
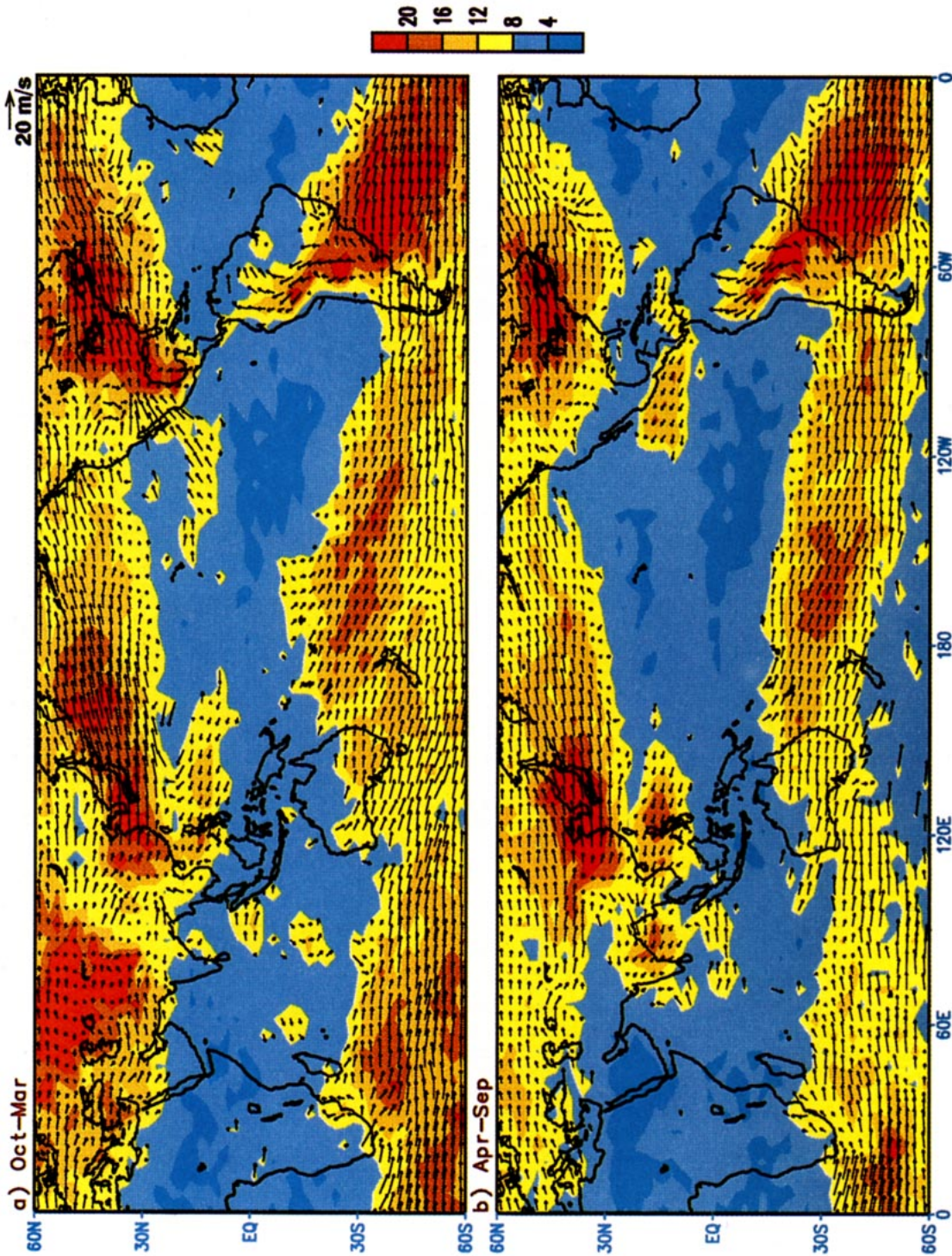
FIG. 4. Distributions of the propagation vectors (arrows, see scale at top right) and temporal coherence (color shading, see scale bar at right) of prominent signals of cloud optical thickness, for (a) October–March and (b) April–September. The results for a given grid point are determined using the positions and values of the extrema P_{-1} and P_{+1} appearing in the composite charts with reference to the grid point in question (see Fig. 3 and the text for details). Vectors are shown only at grid points with temporal coherence exceeding 8.

and North Atlantic is typically 12–15 m s^{-1} in Fig. 4a, and only 7–8 m s^{-1} in Fig. 4b. This seasonal contrast is consistent with the more intense wintertime circulation in these regions (Schubert et al. 1990a, p. 171). The occurrence of highly coherent, eastward-propagating features over much of the extratropical North Pacific and North Atlantic during the cool season is indicative of organized baroclinic waves traveling along the wintertime oceanic "storm tracks" (Blackmon et al. 1977). The typical phase speed of these wave phenomena, as inferred from the satellite data, is in agreement with that estimated by Wallace et al. (1988, their Fig. 8) using geopotential height analyses.

In the Southern Hemisphere, the notable equatorward shift from the warm (Fig. 4a) to the cool season (Fig. 4b) of the region of coherent τ variations in the Australian sector is apparently associated with the establishment of the subtropical jet stream over the Australian landmass during winter (Trenberth 1991, his Fig. 4). The extratropical storm track extending from the Atlantic to the Indian Ocean at approximately 50°S (Trenberth 1991, his Figs. 6 and 7) corresponds to a belt of high temporal coherence in Fig. 4 in both seasons.

The weaker temporal coherence values in the Tropics indicate that much of the τ fluctuations there are poorly organized on timescales of 2–3 days. There are, however, several tropical sites where coherent propagation bears well-defined relationships with the local circulation. Most of the meteorological flow patterns alluded to in the following discussion can be inferred from the 200-mb streamfunction charts compiled in the climatological atlas of Schubert et al. (1990a). During the October–March period (Fig. 4a), the transition from westward propagation east of the Philipines to eastward propagation at points farther north is associated with the stationary upper-level anticyclone over the subtropical western Pacific. The east-northeastward orientation of the arrows from east of Hawaii to Mexico is aligned with the upper-level stationary trough in that region during winter, and may be attributed to the frequent occurrence of cloud "plumes" linking the convective zone in the tropical eastern Pacific to the subtropical jetstream over North America (McGuirk et al. 1988; Kuhnel 1989). Over tropical South America, the propagation vectors east of the Andes are directed northward in both seasons. Also evident in both panels of Fig. 4 are the coherent bands of east-southeastward cloud propagation over the southwestern Pacific and Atlantic at about 30°–40°S, where the South Pacific and South Atlantic convergence zones are located.

During the northern warm season (Fig. 4b), west-northwestward cloud propagation prevails over the tropical regions extending from the western Pacific to the Indian subcontinent, and from the Caribbean to the maritime area off the west coast of Central America, with typical speeds of about 5 m s^{-1}. These zones have also been identified by Lau and Lau (1990) as preferred

sites of synoptic-scale disturbances, with propagation characteristics that are very similar to those obtained in the present study. Another noteworthy feature in Fig. 4b is the change from eastward propagation north of the Tibetan Plateau to westward propagation at points farther south. This phenomenon is apparently related to the upper-level anticyclone residing in this region.

d. Degree of waviness

A measure of the "waviness" of the composite pattern of τ for a given reference site P_0 is provided by the absolute value of the negative extremum appearing in the composite chart of τ on day 0 (e.g., the point N in Figs. 3b and 3e). A site with a large value of this parameter would indicate that enhanced τ at the site is paired with a prominent region of reduced τ in its vicinity. This coexistence of extrema with opposite polarities implies that the overall composite pattern possesses a strong wavelike character. An analogous index (referred to as "teleconnectivity") has been examined by Wallace and Gutzler (1981), Wallace et al. (1988), and Lau and Lau (1990) using one-point teleconnection patterns of geopotential height and vorticity fluctuations. The spatial distributions of the degree of waviness as defined above are displayed in Fig. 5 for (a) North America/North Atlantic during October–March, (b) South America/South Atlantic during April–September and (c) south and east Asia during April–September. The gridpoint values in this figure have been smoothed by the spatial filter described in the previous subsection.

The pattern in Fig. 5a illustrates that the most wavelike disturbances reside along a zonally elongated band from the Great Lakes region to the central North Atlantic. A similar axis of maximum teleconnectivity in geopotential height variations on synoptic timescales has been reported by Wallace et al. (1988, their Fig. 6). A strong degree of waviness is also discernible over the South Atlantic at 45°–50°S (Fig. 5b). The region of relatively high values extending southeastward from the southeastern Brazilian coast is indicative of the wavelike character of the fluctuations in the South Atlantic convergence zone. In agreement with the results presented by Lau and Lau (1990, their Fig. 5), the most wavy disturbances in the tropical Asian sector (Fig. 5c) are found over the Bay of Bengal and the waters surrounding the Philippines.

5. Cloud types and atmospheric circulation associated with extratropical disturbances

a. Procedure for combining composite charts for neighboring sites

To enhance the representativeness of the composite patterns in describing the oceanic extratropical cyclones, an array consisting of 20 reference sites has been chosen separately for the North Atlantic and
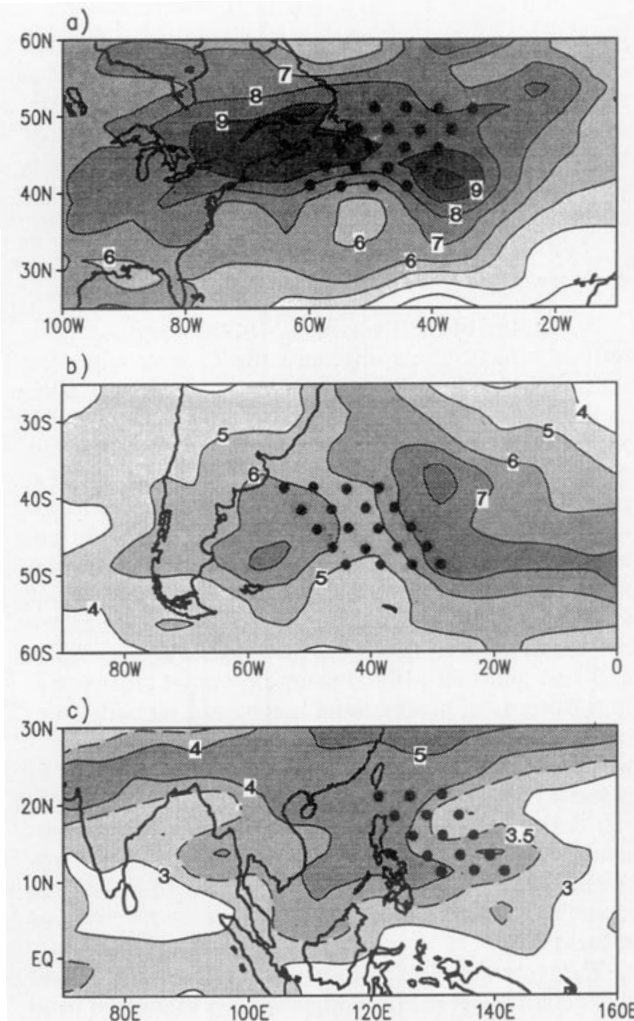
FIG. 5. Distributions of a measure of the waviness of the composite patterns for cloud optical thickness in (a) the North Atlantic and (b) the South Atlantic during their respective cool season, and in (c) south and east Asia during the warm season. This quantity is given by the absolute value of the negative extremum N appearing in the composite chart with reference to individual grid points on the key dates (see Fig. 3 and the text for further details). Interval for solid contours: 1. The arrays of sites used for constructing composite patterns in the latter part of this study are indicated by dots in the respective regions.

South Atlantic (see solid dots in Figs. 5a and 5b). These particular grid points are selected on the basis of the following considerations: they lie in the path of temporally coherent signals of τ with a well-defined direction and speed of propagation (see Fig. 4); and each array covers a contiguous zone with a relatively high degree of waviness (Fig. 5). For the sake of spatial homogeneity, the reference regions thus chosen contain no sharp extrema in the waviness measure.

For each reference site P_0, a composite chart is constructed following the procedure outlined in section 4a, so that altogether 20 composite charts are obtained separately for the North Atlantic and South Atlantic. The

composite data for each P_0 are aligned to a common Cartesian coordinate system. The origin of this system corresponds to the location of P_0. The ordinate and abscissa of this system represent the meridional and zonal displacements (as measured in degrees of latitude and longitude) from P_0, respectively. The entire sample of composite patterns are then combined by arithmetically averaging the 20 composite values at the same coordinates in this common system. Since the actual distance corresponding to a given longitudinal displacement varies with the cosine of the local latitude, the merging of the composite fields associated with reference sites lying in different latitude rows could result in minor distortions of the shape of some of the features, especially in the higher latitudes.

The significance of the signals in the composite patterns presented hereafter has been assessed using the two-tailed Student's t-test. This procedure entails the evaluation of the ratio of the amplitude of these signals versus the local standard deviation of the atmospheric parameter in question. Estimates of the standard deviations have been extracted from the climatological atlases compiled by Lau et al. (1981), Oort (1983), and Schubert et al. (1990b). These computations affirm that a majority of the principal features in the following composite charts exceed the 95% significance level.

The above procedure has been applied to both the ISCCP and ECMWF data. We emphasize here that the composite patterns for all variables being examined in this study are based on key dates determined from the time series of τ at individual reference sites (e.g., see Fig. 2). The merged composite data to be shown in this and the following sections are expressed as departures from a background level, which is defined as the average over the composite data for days -2, -1, 0, $+1$, and $+2$ relative to the key dates.

b. Composite patterns of cloud types and the near-surface circulation

The distributions of different cloud types (color pixels) and the 1000-mb horizontal wind (vectors) and geopotential height (contours), as constructed by merging the corresponding composite charts on day 0 for the 20 reference points in the (a) North Atlantic and (b) South Atlantic during their respective cool seasons, are displayed in Fig. 6.

The sides of each 2.5° × 2.5° grid cell (referred to as a box) in the coordinate system used here are divided into five segments, so as to form 25 smaller squares (hereafter referred to as "pixels"). In a given box, any cloud type with a composite fractional cover above the mean background level is indicated by filling the pixels with the color designated for that cloud type, at the rate of one pixel for each percent increment in cloud cover. To mimic the arbitrary scatter of individual cloud elements constituting the large-scale cloud shield, a random number generator is invoked to decide which spe-
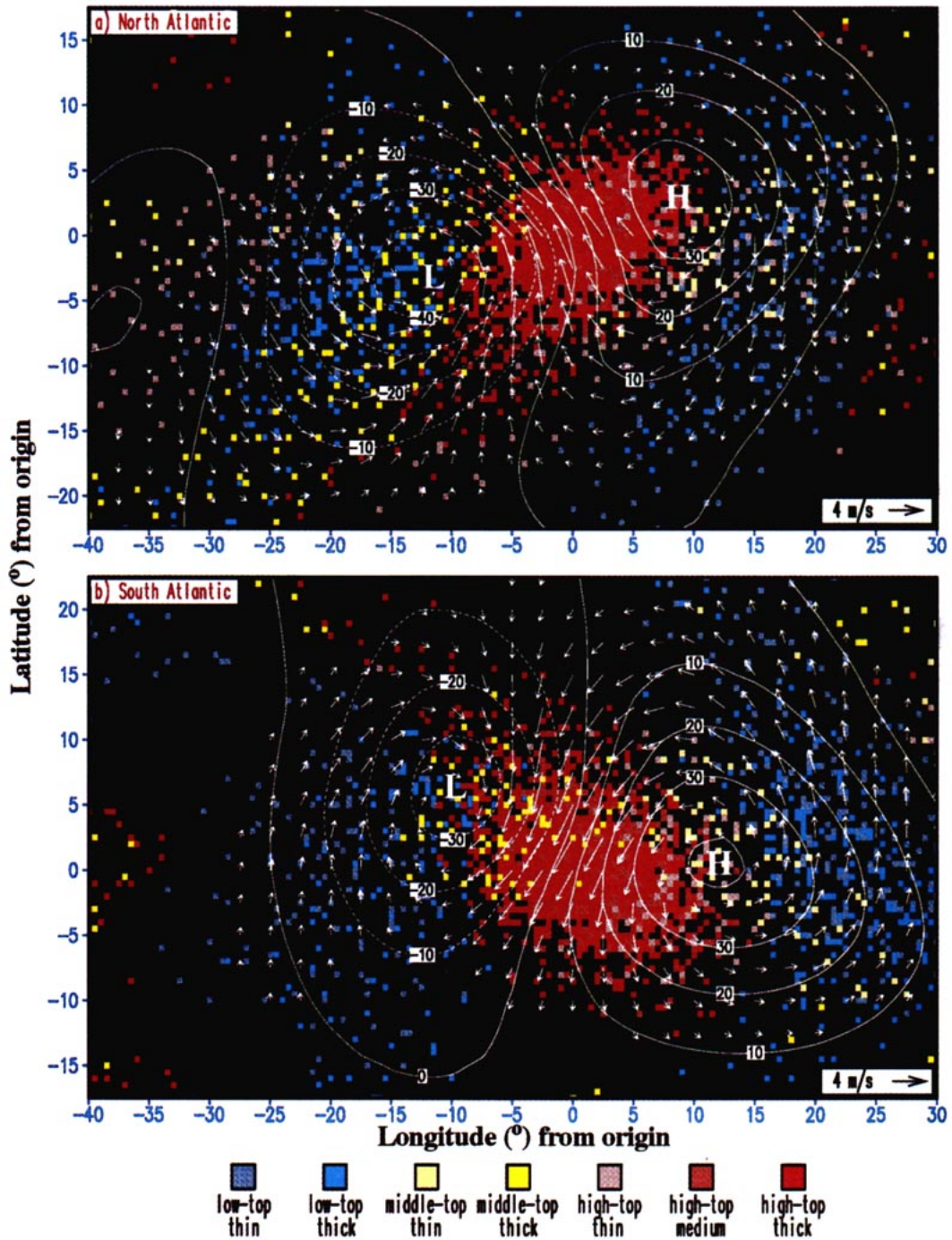
FIG. 6. Distributions of horizontal wind (arrows, see scale at bottom right) and geopotential height (contours, interval: 10 m) at 1000 mb, and of various cloud types (color pixels), as obtained by combining the composite charts (on day 0) based on 20 reference sites in the (a) North Atlantic (see dots in Fig. 5a) and (b) South Atlantic (see dots in Fig. 5b) during their respective cool season. The ordinate (abscissa) of the coordinate system used here corresponds to latitudinal (longitudinal) displacements from the common origin, to which the point P_o for individual reference sites is aligned. Inside each $2.5° \times 2.5°$ grid box of this coordinate system, the presence and relative abundance of a certain cloud type is indicated by plotting a number of randomly scattered pixels with the color designated to the cloud species in question (see legend at bottom and Table 1, and refer to text for further details). Each pixel represents a 1% increment in cloud cover. In this and all following figures, the composite data for the wind, geopotential height, and cloud fields represent deviations from background levels estimated by averaging the values for the 5-day period centered at the key dates.

cific pixels in the 5 × 5 matrix for a given box are to be used for representing a particular cloud type. In cases when the total cloud cover is less than 25% above the background level, those pixels that are not assigned to any cloud species are filled with black.

It is evident from Fig. 6 that the outstanding episodes of large τ at the reference sites are accompanied by well-defined patterns of cloud types and atmospheric circulation. Over the North Atlantic (Fig. 6a), the largest incremental cloud cover is located near the origin (note the almost complete absence of any black pixels in that region). The cloud shield over the reference sites is primarily composed of thick high-top elements, and possesses a tail-like extension toward the southwest of the origin, thus forming a comma-shaped region populated mostly by high-top clouds. The characteristic shape of this zone is similar to that seen in instantaneous satellite images of frontal zones in midlatitudes (e.g., see Carlson 1991, section 10.4). We shall henceforth refer to this zone as the "comma region." There is a notable tendency for thin high-top pixels to occur along the eastern edge of the comma region. The largest concentration of middle-top clouds resides within an elongated zone that is parallel to, but displaced westward from, the comma region. Low-top clouds are found both to the west of the middle-top clouds mentioned above, and approximately 10°–15° east of the comma region. The overall cloud pattern conforms with the classical model of extratropical cyclone structure (Bjerknes and Solberg 1926) and with descriptive accounts of the cloud patterns associated with these frontal systems (e.g., see Wallace and Hobbs 1977, their Fig. 5.38).

The spatial pattern of cloud types in Fig. 6a is seen to be closely related to that of the local atmospheric structure and circulation. The comma region is situated between a low pressure center (denoted by the symbol "L") to its southwest, with a counterclockwise circulation, and a high pressure center (denoted by "H") with a clockwise flow pattern to the northeast. Southerly or southeasterly flows originating from lower latitudes prevail in the high-top cloud shield. The middle-top cloud band extends southwestward from the low center and is aligned with the inflection points of the geopotential contours in the southwestern quadrant of that cyclone. Most of the low-top clouds are found amidst the cold, northerly, or northwesterly airstreams located behind the low center and ahead of the high center. The well-defined spatial relationships between the composite features derived from the independent ISCCP and ECMWF datasets, and the consistency of these relationships with the well-documented behavior of extratropical cyclones, offer strong confirmation of the reliability of the cloud detection algorithms used in producing the ISCCP analyses.

The composite patterns for the cloud and surface circulation fields over the South Atlantic (Fig. 6b) exhibit many similarities to their counterparts in the Northern

Hemisphere (Fig. 6a). Particularly noteworthy are the comma-shaped region of high-top clouds between the high and low pressure centers, the gradual lowering of the cloud ceiling as one traverses westward from the reference site at the origin, and the association of poleward (equatorward) air motion with high (low) cloud tops. Considering the limited in situ observations incorporated in the ECMWF data assimilation system over the South Atlantic, the spatial correspondence between the cloud and circulation features in Fig. 6b is rather remarkable and serves as an independent quality check of both the ECMWF and ISCCP products in such data-sparse regions.

c. Composite patterns of atmospheric circulation and dynamical forcing at representative altitudes

The composite patterns of the horizontal wind vector (arrows) are shown in Fig. 7 at (a) 200, (b) 500, and (c) 1000 mb. Superposed on these vector fields are contours depicting the (a) horizontal advection of absolute vorticity, (b) negative pressure velocity, and (c) horizontal advection of temperature at the corresponding levels. All patterns are based on the key dates identified by the fluctuations of τ at 20 reference sites in the North Atlantic for the cool season, and represent departures of the composite values on day 0 from the average over the 5-day periods centered on the key dates (see details in section 5a). The color cloud pixels in Fig. 6a are reproduced in all three panels in Fig. 7.

Comparison between the vector patterns in the three panels of Fig. 7 reveals that the anticyclonic center is systematically displaced westward with increasing altitude, so that the high-top clouds in the comma region are collocated with strengthened westerlies on the northern flank of a high pressure ridge in the upper troposphere. The latter result is consistent with the frequently observed occurrence of the upper-level jet-stream along the poleward periphery of the comma cloud shield associated with extratropical cyclones (Carlson 1980). Advection by the southerly flow on the eastern flank of the 500-mb trough (which is also displaced westward relative to the surface cyclone) may be a contributing factor for the poleward penetration of middle-top clouds at −10° longitude in the coordinate system used here. Analogously, advection by the northerly flow situated to the west of the 200-mb trough may account for the enhanced equatorward protrusion of thin high-top pixels near −40° longitude.

The contour fields in Fig. 7 are intended for illustrating the contribution of various dynamical forcing mechanisms to the vertical motion field, which is in turn a principal governing factor of the cloud-type distribution. As can be inferred from the quasigeostrophic omega equation (e.g., see Holton 1992, chapter 6), midtropospheric rising motion is associated with an increase of vorticity advection with height (which is mainly due to positive vorticity advection in the upper
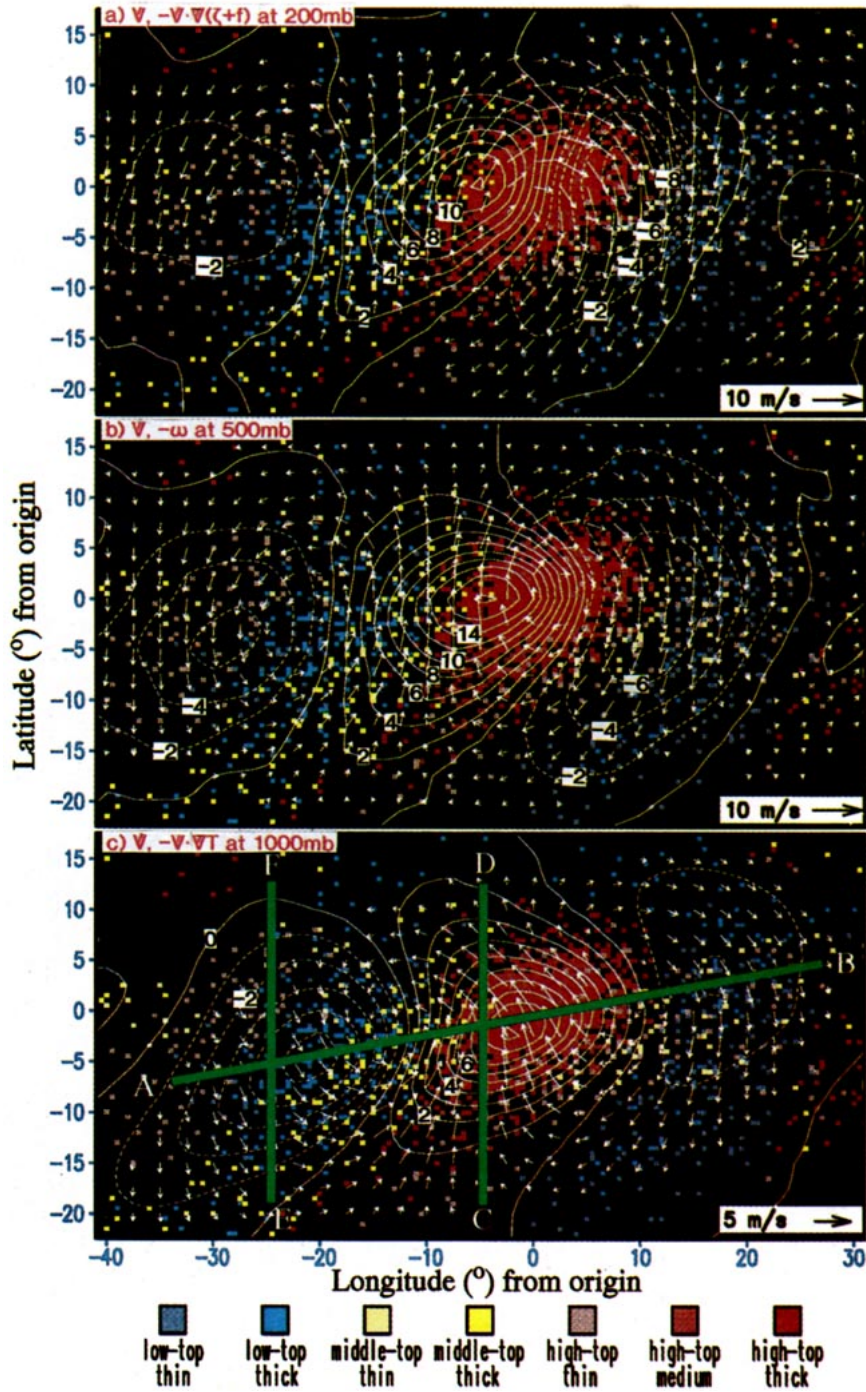
NORTH ATLANTIC

FIG. 7. As in Fig. 6a but for distributions in the North Atlantic region of the (a) advection of absolute vorticity, $-\mathbf{V} \cdot \nabla (\zeta + f)$, (contours, interval: $2 \times 10^{-10} \, \mathrm{s}^{-2}$) and horizontal wind (arrows, see scale at bottom right) at 200 mb; (b) negative pressure velocity, $-\omega$, (contours, interval $2 \times 10^{-2} \, \mathrm{Pa} \, \mathrm{s}^{-1}$, positive values indicate rising motion) and horizontal wind (arrows) at 500 mb; and (c) advection of temperature, $-\mathbf{V} \cdot \nabla T$, (contours, interval: $1 \times 10^{-5} \, ^\circ\mathrm{C} \, \mathrm{s}^{-1}$) and horizontal wind (arrows) at 1000 mb. The cloud pattern (color pixels) in Fig. 6a is superposed on each of the panels. The green line segments in panel (c) indicate the positions of the vertical cross sections to be shown in Figs. 8 and 9.

troposphere), and with warm temperature advection (which attains largest amplitudes near the surface). Conversely, subsidence is forced by negative upper-level vorticity advection, and by cold temperature advection.

For the synoptic-scale wave motions considered here, the total vorticity advection is primarily determined by the advection of relative vorticity (Holton 1992). Hence the contour pattern in Fig. 7a shows positive vorticity advection (which is associated with rising motion) east of the upper-level trough, and negative advection (sinking motion) east of the ridge.

It is evident from the pattern in Fig. 7c that the entire comma region is coincident with warm advection by the poleward moving air masses at 1000 mb. This relationship implies that the rising motion driven by low-tropospheric thermal advection is in phase with the high-top clouds. Cold advection by northerly flows is seen to prevail at a half-wavelength both to the east and the west of the comma region. The resulting subsidence in these cold sectors of the frontal system leads to the formation of low-top clouds. The surface trough axis is aligned with the boundary between the sectors of warm advection to the east and cold advection to the west. This boundary is populated mostly by middle-top clouds. The composite pattern for advection of water vapor at 1000 mb (not shown) is similar to that for temperature advection in Fig. 7c, with positive moisture advection in the comma region, and dry advection in the cold sector.

The composite chart of the 500-mb pressure velocity data extracted from the ECMWF archives, shown in Fig. 7b, appears to receive comparable contributions from temperature and vorticity advections. For instance, the longitudinal phase of the major features in the contour pattern in Fig. 7b is approximately given by the average of the corresponding phases deduced from Figs. 7a and 7c. The comma region is noticeably displaced eastward from the center of rising motion. One probable cause of this displacement is the advective effect exerted by the enhanced eastward motion in the upper troposphere (see arrows embedded in the comma region in Fig. 7a) on the high-top clouds forming in this region of ascending air.

Similar charts of the three-dimensional motion and advection terms at various pressure levels have been constructed on the basis of reference points located in the South Atlantic. All salient relationships among the cloud types, atmospheric circulation, and advective processes, as described in this subsection for the North Atlantic, are well reproduced in the latter patterns (not shown).

d. Composite patterns along vertical planes

To provide a more detailed description of the vertical structure of the features noted in the preceding subsections, composite charts of selected variables are com-

piled at each of the available pressure levels by following the procedure described in section 5a, and vertical cross sections of these composite data are then taken along appropriate horizontal line segments. The segments chosen to illustrate the typical wave structure over the North Atlantic are indicated in Fig. 7c using green lines. The segment labeled AB, which passes through the principal surface high and low centers, is intended for depicting the vertical variations along a full wavelength of the disturbance. The north–south-oriented segments labeled CD and EF are used to portray the pertinent features along the meridional planes corresponding to the warm and cold sectors of the frontal system, respectively.

The contour fields in Fig. 8 describe the distributions of (a) geopotential height, (b) temperature, and (c) negative pressure velocity as functions of pressure (ordinate) and distance along the segment AB (abscissa, with the extreme left and right of this axis corresponding to points A and B, respectively). In constructing these fields, averages are taken over grid points lying within 2.5° of latitude from the green line. Superposed on these patterns are pictorial depictions of the typical cloud-top altitude and τ of the dominant cloud type at various points along AB, as deduced from the ISCCP data for individual atmospheric layers. The upper boundary of the prevalent cloud cover is indicated by scalloping at the appropriate altitude. Thick and thin linings of the cloud tops denote high and low values of τ, respectively. We emphasize here that the scalloping portrays the approximate *cloud ceiling* only, and is not intended to convey any information on the *vertical extent* of the clouds. Description of the latter aspect requires knowledge of the cloud base altitude, as well as detection of the possible presence of multiple cloud decks. As pointed out in section 2, such information is difficult to obtain using satellite measurements.

The contour patterns in Fig. 8 exhibit many familiar structural characteristics of a baroclinic wave (e.g., see Wallace and Hobbs 1977, their Fig. 9.13; Lim and Wallace 1991). The thick high-top clouds within the comma region are coincident with the upper-level ridge (Fig. 8a) and are displaced eastward of the tropospheric maxima in temperature (Fig. 8b) and rising motion (Fig. 8c). Thin high-top clouds are observed near the eastern fringe of the comma zone. The cloud elements found in locations still farther east of this cloud shield mostly have small τ values, with tops being located in the middle and lower troposphere. These thin low-top clouds are situated just east of the surface high pressure center and are under the influence of cold, subsiding air. The cloud pattern west of the comma region is characterized by a systematic reduction of both the cloud-top altitude and τ as one travels westward. For instance, the sky directly above the surface low pressure center is mostly populated with thick
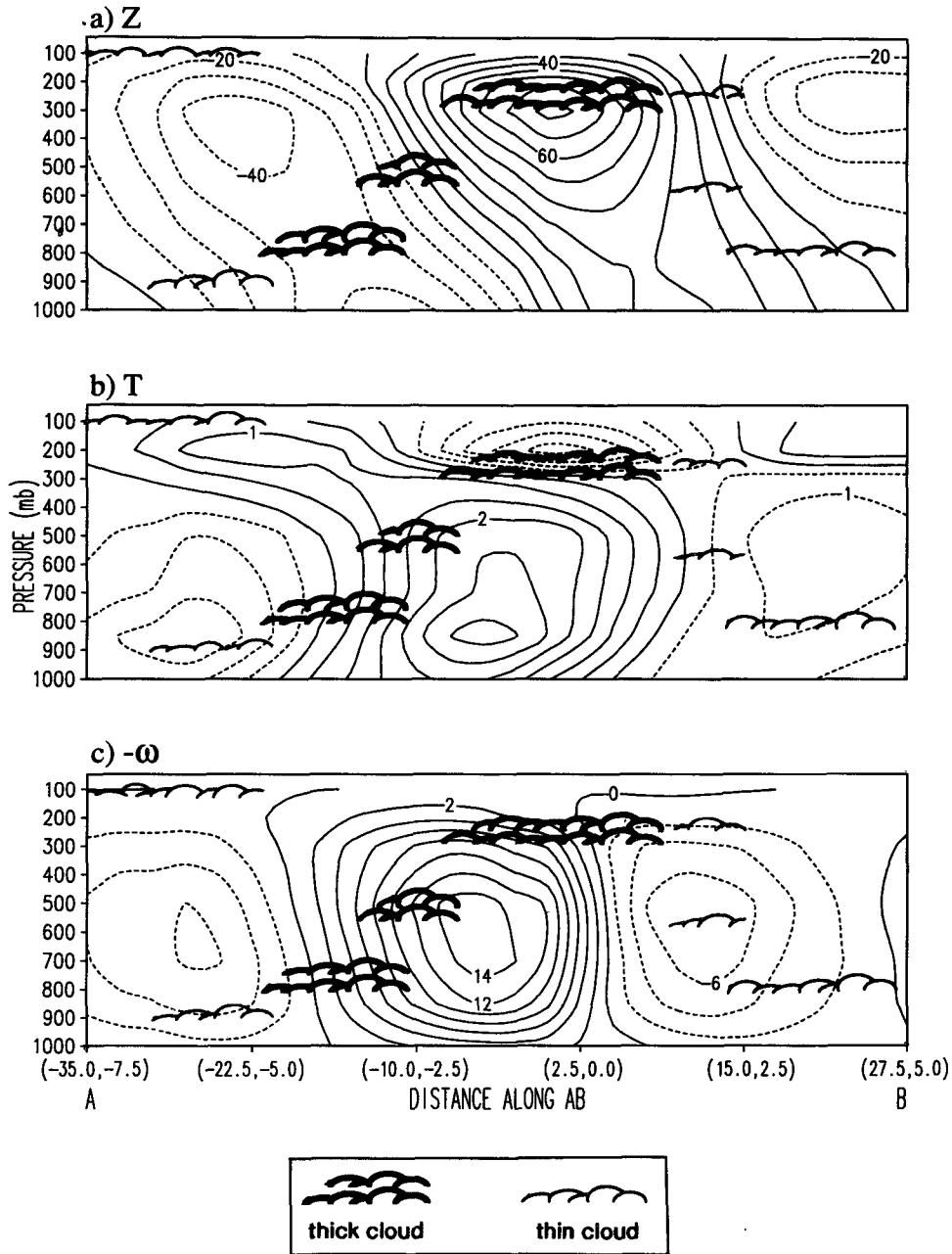
FIG. 8. Distributions (contours) of (a) geopotential height (interval: 10 m); (b) temperature (interval: 0.5°C); and (c) negative pressure velocity, $-\omega$, (interval: 2×10^{-2} Pa s^{-1}, positive values indicate rising motion) in the vertical cross section taken along the North Atlantic line segment labeled AB in Fig. 7c. The extreme left and right of the abscissa correspond to the points A and B, respectively. The pairs of numbers at selected points along the x axis of panel (c) indicate the local abscissas and ordinates (in degrees of longitude and latitude, respectively) with reference to the common coordinate system used in Figs. 6 and 7. Scalloping indicates the cloud-top altitude of the dominant local cloud type. Clouds with large and small optical thicknesses are depicted using thick and thin linings of the cloud tops, respectively (see legend at bottom). No attempt is made to portray the vertical extent of the cloud cover.

middle-top clouds, whereas the skycover behind this low consists mainly of thick low-top clouds, which change to thinner low-top elements in the region still farther west. The distribution of τ is apparently related to the ambient atmospheric temperature and vertical motion. Thick clouds occur preferentially in ascending,

a) WARM SECTOR
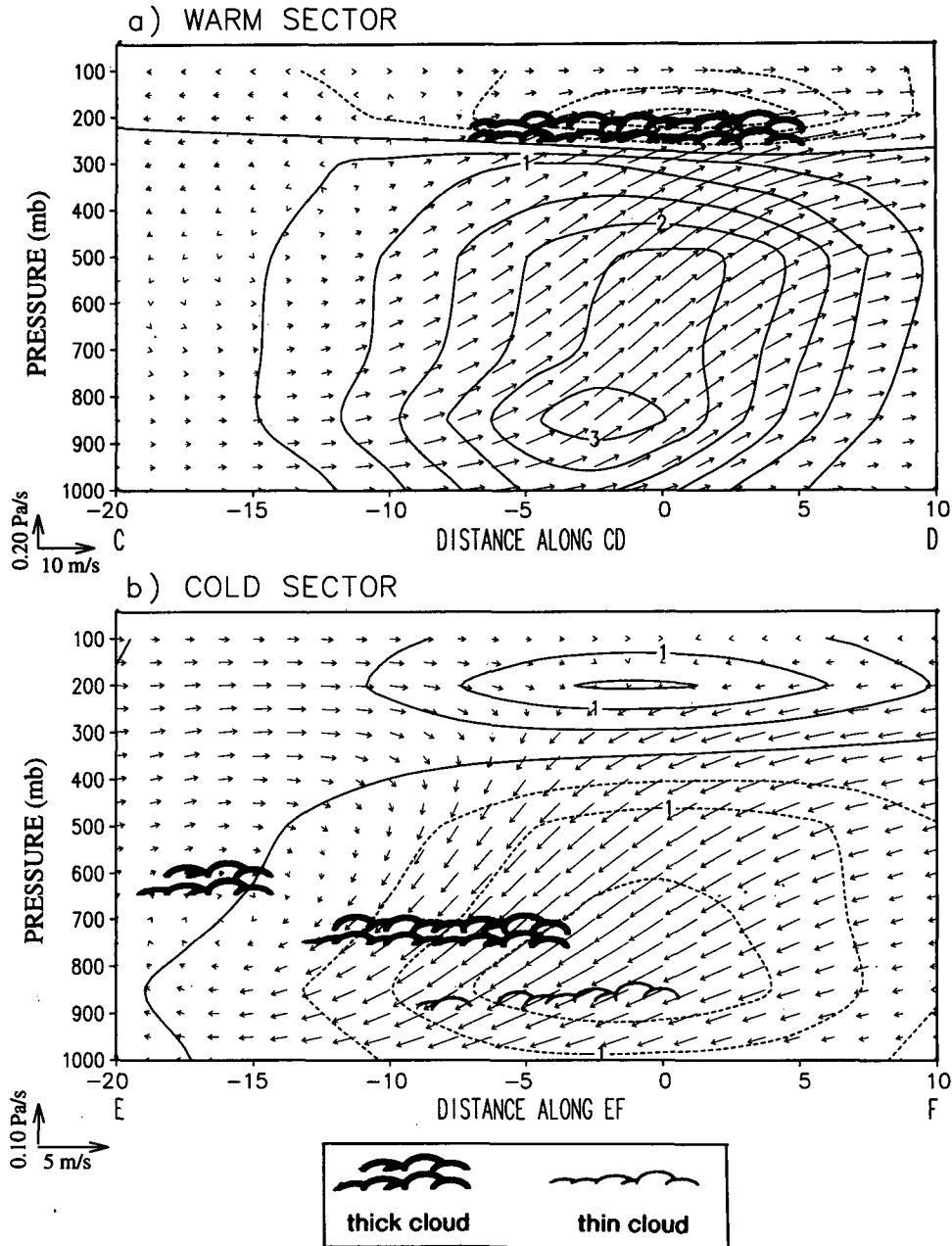
b) COLD SECTOR

thick cloud   thin cloud

FIG. 9. As in Fig. 8 but for distributions of meridional wind and pressure velocity (vectors, see scale at bottom left) and temperature (contours, interval: 0.5°C) in the cross sections taken along the line segments labeled (a) CD (the warm sector), and (b) EF (the cold sector) in Fig. 7c. The extreme left and right of the abscissa correspond to the southern and northern ends of the line segments, respectively. The numbers at selected points along the x axis indicate the local ordinates (in degrees of latitude) with reference to the common coordinate system used in Figs. 6 and 7.

warm air currents, whereas thin clouds are favored in regions of colder temperature and subsidence.

The meridional cross sections in Fig. 9 show the distributions of temperature (contours) and meridional and vertical wind components (vectors), taken along the segments (a) CD in the warm sector and (b) EF in

the cold sector (see green lines in Fig. 7c). Each segment is divided into 13 intervals with a latitudinal width of 2.5°. The composite data shown here are averages over grid points lying within 2.5° of longitude from the green line. The cloud pattern is illustrated using the same convention as that adopted in Fig. 8. Again no

attempt is made to depict the vertical extent of the cloud cover or the presence of multiple cloud decks.

The most notable feature in the circulation along the meridional plane in the warm sector (see arrows in Fig. 9a) is the warm air current originating from the subtropical lower troposphere and reaching much higher altitudes as it advances poleward. The structural and thermal characteristics of the principal air trajectory appearing in Fig. 9a bear some resemblance to those associated with the "warm conveyor belt" in the vicinity of warm fronts, as described in greater detail by Carlson (1980). The most prominent cloud cover in the warm sector is the thick high-top cloud shield, which is situated directly above the region where maximum vertical lifting of the warm conveyor belt takes place.

The patterns of circulation, temperature, and cloud cover described above are almost completely reversed in the cold sector (Fig. 9b). The dominant air current in the latter region has its roots in the subpolar upper troposphere and glides downward as it makes its way to lower latitudes. Much of this trajectory is accompanied by cold temperatures. Low-top clouds prevail under the subsiding air stream.

6. Cloud types and atmospheric circulation associated with tropical disturbances

The procedure described in section 5a has been followed to combine the 15 composite charts based on the individual reference grid points in the tropical western Pacific (see array in Fig. 5c). Each composite chart is constructed by averaging the six most outstanding events identified using the time series of τ for each of the seven available warm seasons (see Fig. 2 and section 3). The results are shown as contours in Fig. 10 for (a) geopotential height at 1000 mb, (b) advection of absolute vorticity at 850 mb, (c) horizontal divergence at 200 mb, and (d) negative pressure velocity at 500 mb. The horizontal wind components at the respective pressure levels are also displayed as vectors in Figs. 10a–c. Superposed on all four panels are color pixels representing the relative proportions of various cloud types. The same plotting technique for constructing the cloud patterns in Figs. 6 and 7 (see also section 5b) is used here, except that each cloud pixel in Fig. 10 corresponds to a 0.5% increment in cloud cover. As in the previous section, all composite data to be presented here are deviations from a background estimated by averaging over the 5-day periods centered at the key dates.

The color pixels in Fig. 10 indicate the presence of a thick high-top cloud shield with a center situated slightly toward the southwest of the origin of the reference coordinate system. This feature (hereafter referred to as the "convective zone") is elongated along an axis orientated from the southwest to the northeast and is accompanied by a similarly shaped low pressure region near the surface (Fig. 10a). The atmospheric

circulation in the vicinity of this cloudy region is characterized by convergent counterclockwise flow at 1000 and 850 mb (Figs. 10a and 10b), divergent anticyclonic outflow at 200 mb toward the east and southeast of the convective center (Fig. 10c), and upward motion at 500 mb (Fig. 10d). Relatively weaker centers of surface high pressure, upper-tropospheric convergence, and midlevel subsidence are discernible toward the northwest and southeast of the convective zone, thus bestowing a weak wavelike appearance to the domain-wide circulation pattern.

As pointed out by Lau and Lau (1992, section 4), the propagation of synoptic disturbances over the tropical western Pacific is primarily governed by vorticity advection in the lower troposphere, whereas the growth or decay of eddy amplitudes mostly results from stretching effects associated with horizontal divergence. The spatial pattern of vorticity advection at 850 mb (see contours in Fig. 10b) exhibits a quadrature relationship with that of the eddy vorticity field itself (as inferred from the vector pattern in the same panel). For instance, the axis of the vortex is aligned with the zero contour in the vorticity advection pattern, whereas positive (negative) vorticity advection prevails to the northwest (southeast) of the vortex center. The vorticity tendency associated with this advection pattern leads to migration of the vortex toward the northwest, in agreement with the prevalent direction of propagation as deduced from observations of the vorticity (Lau and Lau 1990, their Fig. 6) and τ (Fig. 4 of the present study) fields in this region. A different spatial relationship is noted between the divergence and vorticity fluctuations. Inspection of the vector fields in Figs. 10a and 10b reveals that the vortex in the convective zone is accompanied by horizontal convergence in the lower troposphere. The attendant stretching action would produce a vorticity tendency in phase with the convective center, thus leading to further amplification of the disturbance.

The distribution of cloud types (color pixels) in Fig. 10 indicates a marked asymmetry of the cloud-top altitude with respect to the axis of the convective zone. The region to the north-northwest of this zone is mostly populated by low-top clouds, whereas high-top and middle-top thin elements prevail in the sites located south-southeast of the zone. The low-top clouds in the northwestern quadrant stand in front of the approaching convective center and are under the influence of weak convergence at 200 mb (Fig. 10c) and subsidence at 500 mb (Fig. 10d). On the other hand, the scattered thin middle-top and low-top clouds in the southeastern quadrant are situated near the trailing edge of the convective region and appear to shed from the main cloud mass along the path of the anticyclonic outflow at 200 mb (Fig. 10c). The above organization of cloud types in relation to the convection center is reminiscent of the cloud pattern associated with a tropical oceanic squall line (Zipser 1977, his Fig. 13). These tropical systems
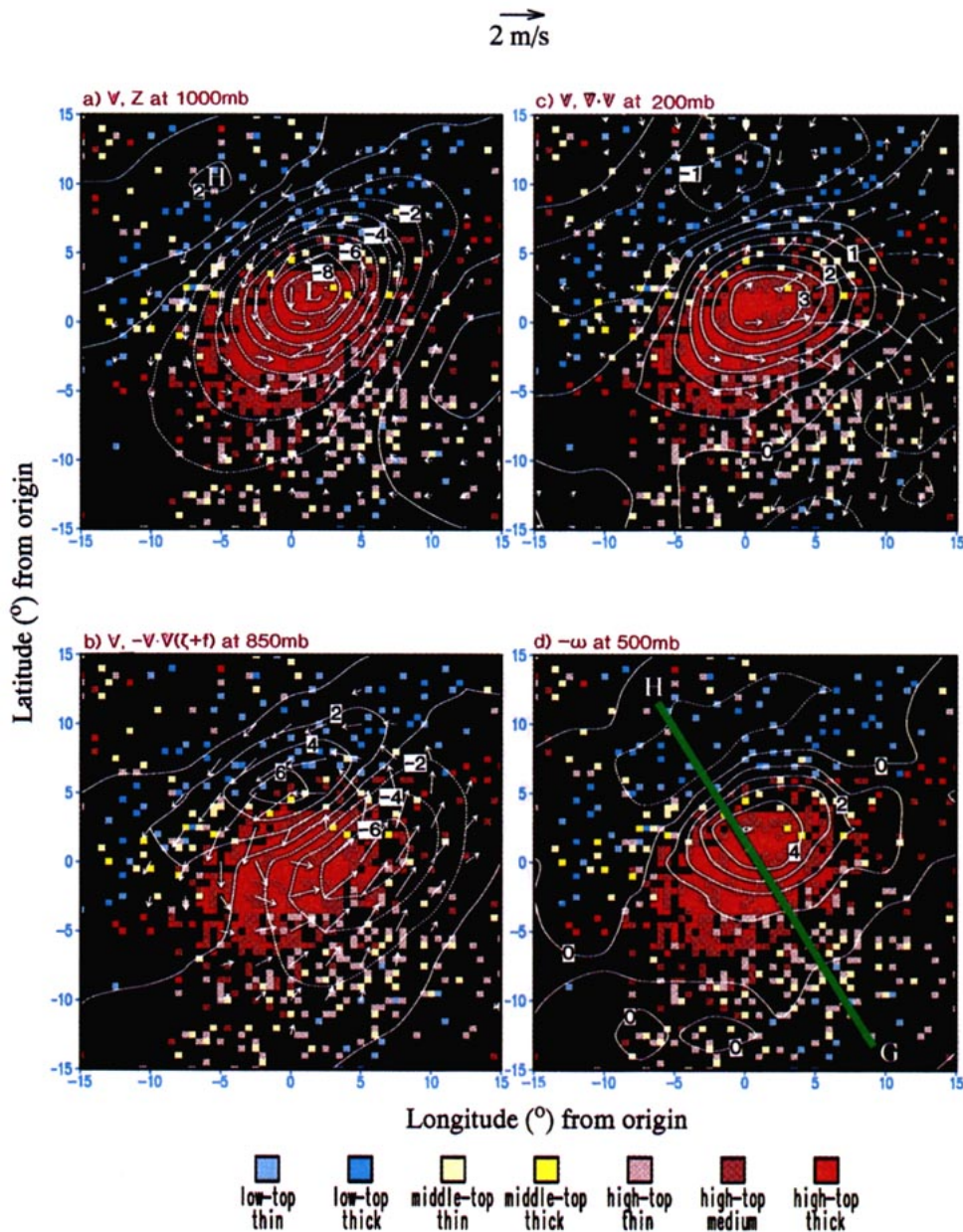
FIG. 10. Distributions of (a) geopotential height (contours, interval: 1 m) and horizontal wind (arrows, see scale at top center) at 1000 mb; (b) advection of absolute vorticity, $-\mathbf{V} \cdot \nabla \, (\zeta + f)$, (contours, interval: 2 $\times \, 10^{-11} \, s^{-2}$) and horizontal wind (arrows) at 850 mb; (c) divergence, $\nabla \cdot \mathbf{V}$, (contours, interval: 5 $\times 10^{-7} \, s^{-1}$) and horizontal wind (arrows) at 200 mb; and (d) negative pressure velocity, $-\omega$, (contours, interval: 1 $\times 10^{-2}$ Pa s^{-1}, positive values indicate rising motion) at 500 mb, as obtained by combining the composite charts (on day 0) based on 15 reference sites in the tropical western Pacific (see dots in Fig. 5c) during the warm season. The ordinate (abscissa) of the coordinate system used here corresponds to latitudinal (longitudinal) displacements from the common origin, to which the point P_0 for individual reference sites is aligned. The distribution of cloud types (color pixels, see legend at bottom) is obtained by the same plotting scheme used in Fig. 6 except that each pixel represents a 0.5% increment in cloud cover. The green line segment in panel (d) indicates the position of the vertical cross section to be shown in Fig. 11.

are typically accompanied by low clouds lying just ahead of the advancing convective towers, and by a high-level anvil spreading toward the rear with gradually decreasing optical thickness.

Trenberth (1992) noted that different changes in the operational system that produced the ECMWF analyses during the 1980s have resulted in spurious trends in the tropical divergent wind and vertical motion fields. To evaluate the impact of such changes on the patterns presented in Figs. 10c and 10d, composite charts for the 200-mb divergence and 500-mb pressure velocity have been constructed using ECMWF data for individual years in the 1983–90 period. The spatial patterns of the latter charts (not shown) are qualitatively similar to the 7-yr averages displayed in Fig. 10. However, the amplitudes of the extrema in the yearly patterns exhibit a noticeable increase with time. Specifically, the level of peak divergence and upward motion near the convective center changes from approximately 2×10^{-6} s^{-1} and 2.5×10^{-2} Pa s^{-1} during 1984–85, to 2.5×10^{-6} s^{-1} and 3.5×10^{-2} Pa s^{-1} during 1986–88, and finally to 5×10^{-6} s^{-1} and 8×10^{-2} Pa s^{-1} during 1989–90.

To illustrate in greater detail the vertical variations of the cloud cover and atmospheric structure, a cross section is taken along the green line labeled as GH in Fig. 10d. This line segment is subdivided into 11 equal intervals, and averages are taken over grid points lying within 2.5° longitude from the green line. The projection of the three-dimensional air motion on the plane of this cross section is shown as arrows in Fig. 11, and the temperature field is presented as contours in the same diagram. The ceiling and τ of the dominant local cloud types are depicted in a manner similar to that in Figs. 8 and 9.

It is evident from Fig. 11 that the strongest rising motion occurs within an atmospheric column that is topped by high, optically thick clouds. The airflow in the vicinity of this column is characterized by convergence in the low and middle troposphere, and divergence near the tropopause. The strongest temperature changes are also observed in the convective column, with negative deviations below 600 mb, and positive deviations at higher levels. This thermal structure is in agreement with that documented by Reed et al. (1977, their Fig. 9b) and Lau and Lau (1990, their Fig. 16d) for such phenomena. The cloud-top altitude is markedly lower in the subsidence region ahead of the leading edge of the convection zone (i.e., the right side of Fig. 11). The optical thickness of the high-top cloud elements is reduced near the trailing edge of the convective center and in the region of outflow from this center. The gross characteristics of the circulation depicted in Fig. 11 are consistent with the synoptic-scale aspects of the streamflow patterns in squall-line systems, as described by Johnson et al. (1990, their Fig. 7) and Houze (1993, his Fig. 9.13).

7. Discussion

An extensive literature on the structural properties of synoptic-scale circulation systems already exists. The present work augments previous studies on this subject by examining in detail the spatial relationships between satellite-derived cloud types and various aspects of the local flow pattern, so as to delineate the interactions between atmospheric dynamics and cloud formation processes. The findings reported herein demonstrate that such interactions in the extratropical disturbances are notably different from those occurring in the tropical zone. Cloud variations over the midlatitude storm tracks are primarily associated with the passage of developing baroclinic waves. The composite charts for these disturbances offer concrete evidence that there is a distinct eastward displacement of the high-top clouds from the center of upward motion at 500 mb (see Figs. 7b and 8c). As pointed out in section 5c, this behavior may be attributed to the advective effects of the intensified westerly flow in the upper troposphere (Fig. 7a). The tendency for the most intense precipitation (which should coincide with the region of maximum ascent) to arrive after the appearance of high-top clouds is in accord with the common experience of weather observers of extratropical cyclones. On the other hand, the cloud pattern in the Tropics is apparently more related to the characteristic structure of convective squall lines, in which the feedbacks between condensational heating and thermally direct circulations play a dominant role. Such distinctions in the dynamical origin of cloud cover in various circulation systems have implications on the modeling of cloud properties in different geographical regions. The results presented here suggest that the fidelity of cloud simulations in large-scale climate models can be enhanced by exploiting the demonstrable synoptic control of the cloud distribution by the local atmospheric flow pattern.

Throughout this study, we have used a simple composite technique that is based solely on the timing of the prominent episodes of large τ (e.g., see the pointers in Fig. 2). This procedure provides the pertinent cloud and circulation fields with considerable freedom to reveal their own characteristic spatial patterns. By using the τ values as the criterion for identifying the key dates, our composite technique tends to preferentially include those weather systems that produce thick and spatially extensive cloud cover, such as extratropical disturbances with pronounced warm fronts. Due to the superposition of many events with varying structures and life histories, as well as the limited spatial resolution of the datasets being used, the detailed temporal development, frontal boundaries, and various mesoscale phenomena seen in individual cases are not evident in the charts shown in Figs. 6–11. However, the virtue of these composite patterns lies in their representativeness of those characteristics that are common to a multitude of prominent cloud episodes.
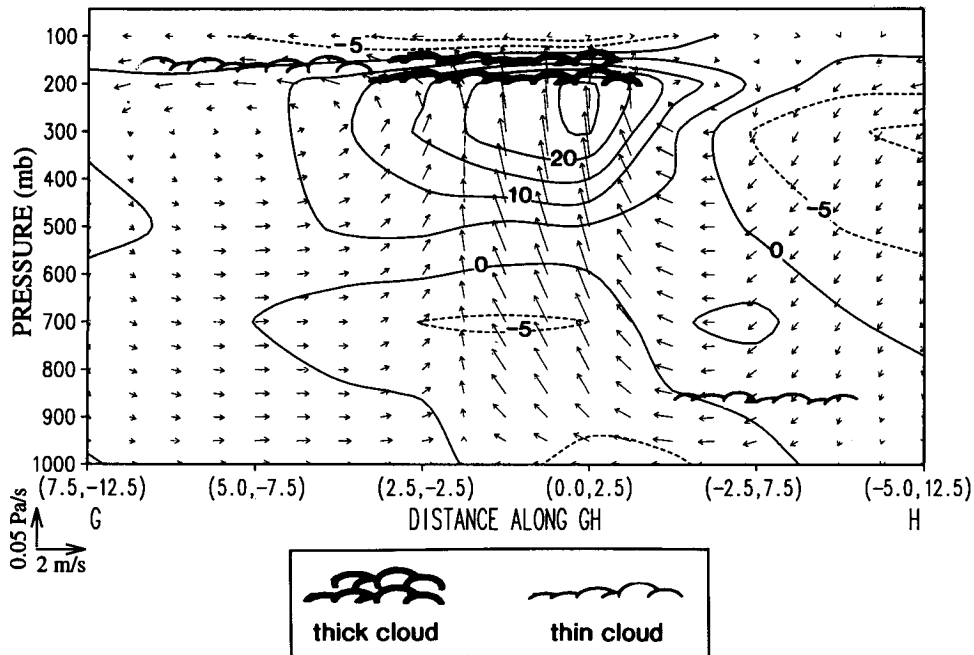
FIG. 11. Distributions of the vector wind (arrows, see scale at bottom left) and temperature (contours, interval: 0.05°C) in the vertical cross section taken along the tropical western Pacific line segment labeled GH in Fig. 10d. The extreme left and right of the abscissa correspond to the points G and H, respectively. The pairs of numbers at selected points along the x axis indicate the local abscissas and ordinates (in degrees of longitude and latitude, respectively) with reference to the common coordinate system used in Fig. 10. The typical cloud-top altitude and optical thickness are indicated using the same illustration scheme as in Figs. 8 and 9. No attempt is made to portray the vertical extent of the cloud cover.

Our study demonstrates the usefulness of satellite cloud observations for diagnosing various aspects of the atmospheric circulation. However, the satellite information is somewhat limited in its ability to detect the occurrence of multiple cloud decks and the altitude of the cloud base. These limitations may be partially removed by examining synoptic reports of the cloud cover from ships and land stations, such as those processed by Warren et al. (1986, 1988). Composite analyses of these reports would yield an alternative description of the cloud organization as viewed from the earth's surface. The latter results would be complementary to the space-based perspective being offered in the present study and would serve as independent checks of the relationships between the cloud and circulation features noted here.

We have thus far devoted much of our efforts to the organization of cloud cover in well-documented circulation systems such as midlatitude cyclone waves and tropical convective disturbances. The global survey of cloud-type climatology conducted in section 3 offers other candidates for further investigations, chief among which are the high-top convective clouds over land during the warm season, and the low-top stratus decks over the subtropical maritime areas. The synoptic situation and atmospheric processes associated with these cloud regimes could conceivably be studied by examining the

satellite cloud products in conjunction with conventional meteorological datasets, using analysis tools similar to those developed in this and other works. By the same token, our current emphasis on phenomena with timescales of several days could also be broadened to include intraseasonal and interannual fluctuations of cloud amount, and to assess the roles of different internal and boundary mechanisms in cloud variability on such timescales.

The spatial resolution (~280 km) of the satellite dataset used in the present study is adequate for examining synoptic-scale atmospheric features. However, a more detailed investigation of the mesoscale phenomena embedded in these features would require datasets with considerably finer resolution. Some high-definition satellite products already exist. For instance, selected satellite measurements are currently archived at the level of individual pixels (with dimensions of several kilometers), and the B3 analyses produced by ISCCP provide radiance information on spatial scales of approximately 30 km (see Rossow et al. 1987). With the continuing advance of remote sensing techniques, data retrieval methodology, and capacity for storing and transmitting information, it is anticipated that subsynoptic-scale satellite analyses with near-global coverage will become even more accessible in the near future. The potential of these new data re-

sources for diagnosing the fine structure of various atmospheric phenomena needs to be explored further. The current study demonstrates that one viable way of realizing this potential is to examine the satellite observations in combination with independent analyses of the ambient atmospheric circulation and structure, and to interpret the relationships between the two sets of data fields on the basis of our empirical and theoretical knowledge.

REFERENCES

Bjerknes, J., and H. Solberg, 1926: Life cycle of cyclones and the polar front theory of atmospheric circulation. *Geofys. Publ.,* **3**, 1–18.

Blackmon, M. L., J. M. Wallace, N.-C. Lau, and S. L. Mullen, 1977: An observational study of the Northern Hemisphere wintertime circulation. *J. Atmos. Sci.,* **34**, 1040–1053.

——, Y.-H., Lee, J. M. Wallace, and H-H. Hsu, 1984: Time variation of 500 mb height fluctuations with long, intermediate and short time scales as deduced from lag-correlation statistics. *J. Atmos. Sci.,* **41**, 981–991.

Bluestein, H. B., 1992: *Synoptic–Dynamic Meteorology in Midlatitudes.* Vol. 1, *Principles of Kinematics and Dynamics,* Oxford University Press, 431 pp.

——, 1993: *Synoptic–Dynamic Meteorology in Midlatitudes.* Vol. 2, *Observations and Theory of Weather Systems,* Oxford University Press, 594 pp.

Carlson, T. N., 1980: Airflow through midlatitude cyclones and the comma cloud pattern. *Mon. Wea. Rev.,* **108**, 1498–1509.

——, 1991: *Mid-latitude Weather Systems.* Harper Collins, 507 pp.

Deser, C., J. J. Bates, and S. Wahl, 1993: The influence of sea surface temperature gradients on stratiform cloudiness along the equatorial front in the Pacific Ocean. *J. Climate,* **6**, 1172–1180.

Emanuel, K. A., 1994: *Atmospheric Convection.* Oxford University Press, 580 pp.

Evans, M. S., D. Keyser, L. F. Bosart, and G. M. Lackmann, 1994: A satellite-derived classification scheme for rapid maritime cyclogenesis. *Mon. Wea. Rev.,* **122**, 1381–1416.

Fu, R., A. D. Del Genio, and W. B. Rossow, 1990: Behavior of deep convective clouds in the tropical Pacific deduced from ISCCP radiances. *J. Climate,* **3**, 1129–1152.

——, ——, and ——, 1994: Influence of ocean surface conditions on atmospheric vertical thermodynamic structure and deep convection. *J. Climate,* **7**, 1092–1108.

Hartmann, D. L., M. E. Ockert-Bell, and M. L. Michelsen, 1992: The effect of cloud type on earth's energy balance: Global analysis. *J. Climate,* **5**, 1281–1304.

Holloway, J. L., Jr., 1958: Smoothing and filtering of time series and space fields. *Advances in Geophysics,* Vol. 4, Academic Press, 351–389.

Holton, J. R., 1992: *An Introduction to Dynamic Meteorology.* 3rd ed. Academic Press, 511 pp.

Houze, R. A., Jr., 1993: *Cloud Dynamics.* Academic Press, 573 pp.

Ison, N. T., A. M. Feyerherm, and L. D. Bark, 1971: Wet period precipitation and the gamma distribution. *J. Appl. Meteor.,* **10**, 658–665.

Johnson, R. H., W. A. Gallus Jr., and M. D. Vescio, 1990: Near-tropopause vertical motion within the trailing-stratiform region of a midlatitude squall line. *J. Atmos. Sci.,* **47**, 2200–2210.

Klein, S. A., and D. L. Hartmann, 1993: The seasonal cycle of low stratiform clouds. *J. Climate,* **6**, 1587–1606.

Kuhnel, I., 1989: Tropical–extratropical cloudband climatology. *Int. J. Climatol.,* **9**, 441–463.

Lau, K.-H., and N.-C. Lau, 1990: Observed structure and propagation characteristics of tropical summertime synoptic scale disturbances. *Mon. Wea. Rev.,* **118**, 1888–1913.

——, and ——, 1992: The energetics and propagation dynamics of tropical summertime synoptic-scale disturbances. *Mon. Wea. Rev.,* **120**, 2523–2539.

Lau, N-C., G. H. White, and R. L. Jenne, 1981: Circulation statistics for the extratropical Northern Hemisphere based on NMC analyses. NCAR Tech. Note 171 + STR, 138 pp.

Lim, G. H., and J. M. Wallace, 1991: Structure and evolution of baroclinic waves as inferred from regression analysis. *J. Atmos. Sci.,* **48**, 1718–1732.

McGuirk, J. P., A. H. Thompson, and J. R. Schaeffer, 1988: An eastern Pacific tropical plume. *Mon. Wea. Rev.,* **116**, 2505–2521.

Nitta, T., and Y. Takayabu, 1985: Global analysis of the lower tropospheric disturbances in the Tropics during the northern summer of the FGGE year. Part II: Regional characteristics of the disturbances. *Pure Appl. Geophys.,* **123**, 272–292.

——, Y. Nakagomi, Y. Suzuki, N. Hasegawa, and A. Kadokura, 1985: Global analysis of the lower tropospheric disturbances in the Tropics during the northern summer of the FGGE year. Part I: Global features of the disturbances. *J. Meteor. Soc. Japan.,* **63**, 1–19.

Ockert-Bell, M. E., and D. L. Hartmann, 1992: The effect of cloud type on earth's energy balance: Results for selected regions. *J. Climate,* **5**, 1157–1171.

Oort, A. H., 1983: Global atmospheric circulation statistics, 1958–1973. NOAA Prof. Paper 14, 180 pp.

Reed, R. J., D. C. Norquist, and E. E. Recker, 1977: The structure and properties of African wave disturbances as observed during phase III of GATE. *Mon. Wea. Rev.,* **105**, 317–333.

——, E. Klinker, and A. Hollingsworth, 1988: The structure and characteristics of African easterly wave disturbances as determined from the ECMWF operational analysis/forecast system. *Meteor. Atmos. Phys.,* **38**, 22–33.

Rossow, W. B., and R. A. Schiffer, 1991: ISCCP cloud data products. *Bull. Amer. Meteor. Soc.,* **72**, 2–20.

——, and L. C. Garder, 1993a: Cloud detection using satellite measurements of infrared and visible radiances for ISCCP. *J. Climate,* **6**, 2341–2369.

——, and ——, 1993b: Validation of ISCCP cloud detections. *J. Climate,* **6**, 2370–2393.

——, E. Kinsella, and A. Wolf, 1987: International Satellite Cloud Climatology Project (ISCCP) description of reduced resolution radiance data. WMO/TD-No. 58, World Meteorological Organization, Geneva, 143 pp.

——, L. C. Garder, P. J. Lu, and A. W. Walker, 1988: International Satellite Cloud Climatology Project (ISCCP) Documentation of Cloud Data. WMO/TD-No. 266, World Meteorological Organization, Geneva, 78 pp.

——, A. W. Walker, and L. C. Garder, 1993: Comparison of ISCCP and other cloud amounts. *J. Climate,* **6**, 2394–2418.

Schiffer, R. A., and W. B. Rossow, 1983: The International Satellite Cloud Climatology Project (ISCCP): The first project of the

World Climate Research Program. *Bull. Amer. Meteor. Soc.,* **64,** 779–784.

Schubert, S., C.-K. Park, W. Higgins, S. Moorthi, and M. Suarez, 1990a: An atlas of ECMWF analyses. Part I—First moment quantities. NASA Tech. Memo. 100747, 258 pp.

——, W. Higgins, C.-K. Park, S. Moorthi, and M. Suarez, 1990b: An atlas of ECMWF analyses. Part II—Second moment quantities. NASA Tech. Memo. 100762, 262 pp.

Trenberth, K. E., 1991: Storm tracks in the Southern Hemisphere. *J. Atmos. Sci.,* **48,** 2159–2178.

——, 1992: Global analyses from ECMWF and atlas of 1000 to 10 mb circulation statistics. NCAR Tech. Note 373 + STR, 191 pp.

Troup, A. J., and N. A. Streten, 1972: Satellite-observed Southern Hemisphere cloud vortices in relation to conventional observations. *J. Appl. Meteor.,* **11,** 909–917.

Tselioudis, G., W. B. Rossow, and D. Rind, 1992: Global patterns of cloud optical thickness variation with temperature. *J. Climate,* **5,** 1484–1495.

Wallace, J. M., and P. V. Hobbs, 1977: *Atmospheric Science—An Introductory Survey.* Academic Press, 467 pp.

——, and D. S. Gutzler, 1981: Teleconnections in the geopotential height field during the Northern Hemisphere winter. *Mon. Wea. Rev.,* **109,** 784–812.

——, G.-H. Lim, and M. L. Blackmon, 1988: Relationship between cyclone tracks, anticyclone tracks and baroclinic waveguides. *J. Atmos. Sci.,* **45,** 439–462.

Warren, S. G., C. J. Hahn, J. London, R. M. Chervin, and R. L. Jenne, 1986: Global distribution of total cloud and cloud type amounts over land. NCAR Tech. Note TN-273 + STR/DOE Tech. Rep. ER/60085-HI, 29 pp. +200 maps. [NTIS DE87-00-6903.]

——, ——, ——, ——, and ——, 1988: Global distribution of total cloud and cloud type amounts over the ocean. NCAR Tech. Note TN-317 + STR/DOE Tech. Rep. ER-0406, 42 pp. + 170 maps. [NTIS DE90-00-3187.]

Weare, B. C., 1992: Variations in *Nimbus-7* cloud estimates. Part II: Regional changes. *J. Climate,* **5,** 1506–1513.

——, 1993: Multi-year statistics of selected variables from the ISCCP C2 data set. *Quart. J. Roy. Meteor. Soc.,* **119,** 965–985.

——, 1994: Interrelationships between cloud properties and sea surface temperatures on seasonal and interannual time scales. *J. Climate,* **7,** 248–260.

Zipser, E. J., 1977: Mesoscale and convective-scale downdrafts as distinct components of squall-line structure. *Mon. Wea. Rev.,* **105,** 1568–1589.